Optical Techniques for Crude Oil and Asphaltene Characterization

by

Mohamed Matoug
B. Sc., University of Tripoli, 2009

A Thesis Submitted in Partial Fulfillment
of the Requirements for the Degree of

MASTER OF APPLIED SCIENCE

in the Department of Electrical and Computer Engineering

Supervisory Committee

Optical Techniques for Crude Oil and Asphaltene Characterization

by

Mohamed Matoug
B. Sc., University of Tripoli, 2009

Supervisory Committee

Dr. Reuven Gordon, (Department of Electrical and Computer Engineering)
Supervisor

Dr. Thomas Tiedje, (Department of Electrical and Computer Engineering)
Departmental Member

Abstract

Supervisory Committee
Dr. Reuven Gordon, (Department of Electrical and Computer Engineering)
Supervisor
Dr. Thomas Tiedje, (Department of Electrical and Computer Engineering)
Departmental Member

In this work, different optical techniques have been explored to study and characterize crude oil and its asphaltene. Crude oil is extremely complex fluid used to produce fuel for a wide range of applications. The characterization of this fluid is key for optimum operations in the oil and gas industry.

First, we demonstrate the application of gold nanorods in characterizing a different set of crude oils. We utilize the high sensitivity of the Localized Surface Plasmon Resonance (LSPR) of the nanorods to the surrounding environment to measure the crude oil refractive index. We immobilized the nanorods on a glass substrate and took the measurement in a reflection configuration. The setup and the nanorods were calibrated using different fluids with known refractive index, and a sensitivity of 247 nm/RIU and a resolution of 0.013 RIU have been achieved. In addition to the simplicity of this approach, it has eliminated the absorption issue and made it possible to measure high optical density crude oils with typical Visible-NIR wavelengths. Surface-Enhanced Raman Spectra (SERS) can also be measured. SERS can provide additional useful information, especially to some applications such as downhole fluid analysis, where confirmation of the hydrocarbons presence is necessary.

In the second part of this work, we used Terahertz Time-Domain Spectroscopy (THz-TDS) to study the asphaltene in three different crude oils. THz-TDS has a feature of measuring the amplitude and time delay and consequently the refractive index and absorption coefficient spectra simultaneously. Our approach is based on measuring the THz signal from neat crude oil samples and comparing it with the THz signal after removing the asphaltene from the samples (maltene). The results show that the difference in the time delay and the peak amplitude between the neat oil and the maltene have a linear relation with the asphaltene content. The refractive index spectra of different asphaltenes show variation in the low THz frequencies and comparable spectra in the higher frequencies. The absorption of asphaltene was mild and no distinctive absorption feature was observed except for some narrow absorption peaks that we attributed to water molecules adsorbed on the asphaltene.

Table of Contents

List of Tables

List of Figures

Acknowledgments

There are many, whom without their presence in our life, we would not be able to carry on. I appreciate and will never forget everyone's help. Special thanks to:

My supervisor, Dr. Reuven Gordon, for giving me the opportunity to work in his group, mentoring and encouragement throughout my research, and simply being a Man in the low moments. His enthusiasm and ambition in research have made him a true role model for me as a junior researcher. I, indeed, enjoyed working under his supervision.

My parents, Dr. Mahmoud Matoug and Samira Lahmar. When talking about you, words can't do it justice. Thank you for raising me into the person I am today. I am honored that I am your son and will always be grateful for your love and support.

Abdulbaset Shaghluf and Shukria Abuzoda, for raising such a wonderful girl who happens to be my wife. **Nagwa**, my beloved wife, your help in every step of the way has made a huge difference.

Yasmine and Ayat, the journey with them have been absolutely terrific. I cannot wait until you grow up and read this. You have helped me a great deal, and more than anyone else can ever imagine.

My friends in the Nanoplasmonic lab, current and past students, for their help, support, and insightful discussions. Thanks to Afshin for training me on the Terahertz, thanks to Ghazal for training me on her setup, and thanks to Ahmed and Steve for their help prior to their departure.

The University of Tripoli in Libya and NSERC MEET program for funding me throughout my study.

Dedication

To LIBYA

And

All Scientists, Physicists, and Engineers whom their discoveries and innovations made it possible for us today to live unprecedented luxury.

"I swear by the locations of the stars. If you only knew, how tremendous this oath is"
Text from 1400 years ago

Chapter 1 Introduction

1.1 Motivation

Crude oils are the main source of fuel to the energy, industry, heating, and transportation sectors [1]. This substance is key for modern industry. The products extracted from crude oil cover a wide range of applications such as medical materials, construction materials, road surfacing, and plastics. The process of producing crude oil starts with a seismic survey in an area that has the potential of having crude oil and drilling a few exploration wells. Once the oil presence is confirmed, more production wells are drilled, and a network of pipelines is built to transport the oil into refinery stations. This is a lengthy and complicated process before these products can reach the end users [1]. Moreover, it is getting significantly more challenging as many locations in the world are transitioning from light and medium crude oils to heavy and extra heavy crude oils, mainly because of the asphaltenes [2].

The measurement of crude oil refractive index can provide valuable information as refractive index correlates well with different crude oil properties [3,4]. This measurement is not always attainable for heavy and extra heavy crude oils using the conventional refractometers as their optical densities are very high [5]. In this research, we propose the use of gold nanorods as a platform for measuring the crude oil refractive index. Gold

nanorods or nanoparticles, in general, are very sensitive to slight changes in the refractive index of the surrounding environment [6]. The sensitivity of nanoparticles to the change of the refractive index depends on the shape and size of the particle [7]. In addition, gold nanorods can be used for measuring the surface-enhanced Raman spectra of the crude oil [8]. Raman spectroscopy had found little attention in the past in studying crude oil, but with SERS the signal might be stronger and give extra information.

Another crucial parameter in evaluating the crude oil is its asphaltene content. This is important for flow assurance problem prediction and mitigation. It also works as an indicator of the crude oil quality [1,9]. This measurement is done by standardized methods based on diluting the crude oil with alkane solvent and filtration [10-12]. These methods suffer from poor reproducibly, need for a large amount of solvent, and being time-consuming.

In the second part of this research, we study the asphaltene in the crude oil using Terahertz Time-Domain Spectroscopy (THz-TDS). Terahertz technologies are being applied in a wide range of areas such as imaging [13], security [14], medicine [15], communications [16], and spectroscopy [17]. The THz-TDS technique gives information about both the amplitude and phase of the sample under test, which enables us to calculate the real and imaginary part of the refractive index simultaneously with negligible harmful effect on the sample due to the low photon energy of the waves [18,19]. Since optical absorption and refractive index are important for probing different properties of the

asphaltene, it would be beneficial to use a technique that provides both parameters simultaneously such as (THz-TDS).

1.2 Outline of This Thesis

Chapter 1 provides a brief introduction about the crude oil and presents the problems to be addressed in this work and the suggested methods.

Chapter 2 gives a background in some details about the crude oil and asphaltene. It also contains a short literature review on how to characterize these materials.

Chapter 3 covers the underlying theories of experiments used in this work. It includes the localized surface plasmon resonance, surface enhanced Raman spectroscopy, and terahertz spectroscopy.

Chapter 4 explains the materials, the experimental setups, and procedure used in this work.

Chapter 5 presents and discusses the experimental results.

Chapter 6 concludes this work and suggests future work.

Chapter 2 Background

2.1 Crude Oils

Crude oils are a complex chemical mixture of mainly different hydrocarbons. Because of their broad applications, they are considered one of the most important substances consumed in the last century. The crude oil has relatively low value as a raw material but when processed it produces high-value products. For example, gasoline, kerosene, and diesel are the main fuels for transportation. The fuel oil is used in residential heating and electricity generation. Other crude oil products such as lubricants, plastics, paints, and polymers are essential to modern industrial society [1].

Crude oil has remained the largest source of energy in the globe over the past three decades with approximately 33% of the energy in 2016 [20], and will continue to be the largest for at least the next two decades (Figure 1) [21]. Currently, there is a shift toward heavy unconventional crude oil resources such as Canadian oil sands, the extra heavy oil in Venezuela, and the shale oil in the US as conventional oil resources are depleting [2]. These unconventional resources constitute almost two thirds the worldwide oil reserves [20], thus, they exhibit huge economic opportunities. The need to shift to heavy oil, in addition to the environmental concerns, has encouraged many researchers to look for more efficient and safe ways to handle and utilize this substance. Spectroscopic methods have found interest in the field of oil and gas as they provide information at the molecular level. Fluorescence

techniques are widely used for qualitative and quantitative analysis of crude oil due to their sensitivity and selectivity. However, the use of fluorescence is associated with considerable challenges; the most notable one is in making it suitable for any crude oil from different sources [22]. Infrared spectroscopies have been under extensive studies and use in the field of oil and gas for many years [23-25]. With all the advantages that infrared brought to the oilfield industry, there are still limitations associated with this technique [26]. Raman spectroscopy has been limited in studying crude oil as a bulk, mainly because of the intense fluorescence that rises from the aromatic fraction of crude oil [27], but it has been successful in studying some oil fractions such as asphaltene and fuel [28-29].

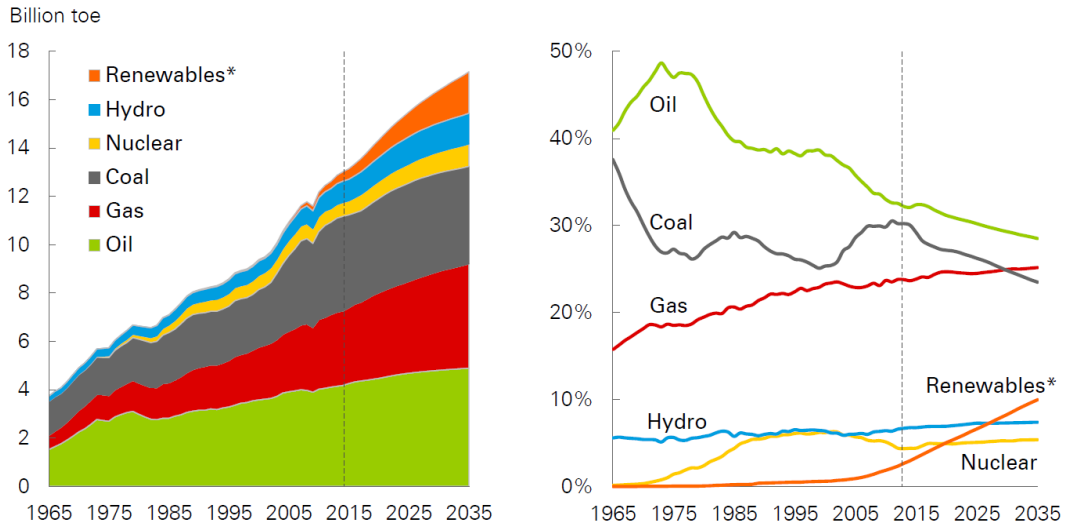

Figure 1: (left) Energy consumption by fuel. (right) Percentage of energy shares [3].

Recently, THz spectroscopy has found its way into petroleum applications in different reports. It has been proven that THz technique can be used to qualitatively identify the source of crude oil among different samples based on the absorption and refractive index spectrum [30]. Other works include detecting the disaggregation of the crude oil particles

in the presence of a magnetic field [31], characterizing wax crystals in waxy crude oil [32], measuring water content in crude oil [33-34], measuring the properties of some crude oil products [35-38], natural gas [39], and coal [40]. All of those have been presented over the past few years.

2.2 Characterization of Crude Oil

Because of its complexity, the characterization of crude oil requires a measurement of various chemical and physical properties. Dealing with heavy oil exhibits further complication than the typical conventional oil. Therefore, the characterization of these heavy oils is a significant element for optimum design and functioning of the production, processing, and transportation equipment. And more importantly, to determine whether it is economically beneficial to produce the oil or not [41]. The following are some of the main measurements that give insight for crude oil characterization.

2.2.1 Crude Oil Density

The density and specific gravity, which is a measure of how heavy the crude oil is compared to water, are the preliminary assessments of the quality of crude oil. The light oil contains more valuable product that can be produced and processed easily, whereas the heavy oil contains more complex components that have much less value and are harder to process. The American Petroleum Institute (API) gravity is the preferred way to express the density of the crude oil in the industry. This property is calculated by this equation:

$$°API = (141.5/\text{Specific Gravity}) - 131.5$$

where the specific gravity is the ratio between the oil and water density. Since water density is 1 g/mL, the specific gravity has the same value as density, but it is a unitless number.

The crude oil can be classified from light to extra heavy according to its API gravity as shown in Table 1 [1].

Table 1: Classification of crude oils according to their API gravity and density [1].

	API Gravity	**Density**
Light crude oil	> 31.1°	< 870 g/ml
Medium crude oil	< 31.1° and > 22.3°	< 920 g/ml and > 870 g/ml
Heavy crude oil	< 22.3° and > 10°	< 1000 g/ml and > 920 g/ml
Extra heavy crude oil	< 10°	> 1000 g/ml

2.2.2 Crude Oil Refractive Index

The measurement of the refractive index has numerous benefits to petroleum engineers. Several thermophysical properties such as density, critical constants, the equation of state parameters, heat capacity, and transport properties can be estimated by the measurement of the refractive index. The refractive index has also been used to assess the composition of undefined petroleum mixtures [3]. The density of the crude oil correlates strongly with the refractive index, and thus, it can be used as an accurate way to estimate the API gravity [4]. The measurement of the refractive index is used to detect the onset of the asphaltene precipitations [42-43]. Based on that, the crude oil refractive index is a useful parameter in characterizing the oil properties.

The measurement of the refractive index can be tricky. One of the challenges in measuring it is the high optical density of crude oil, especially the heavy and extra heavy [44]. As shown in Figure 2, the optical density in the visible range exceeds 4 OD for only 1 mm path length, which means the light transmission through the fluid is not possible for refractive index measurements except for light and medium oils [44].

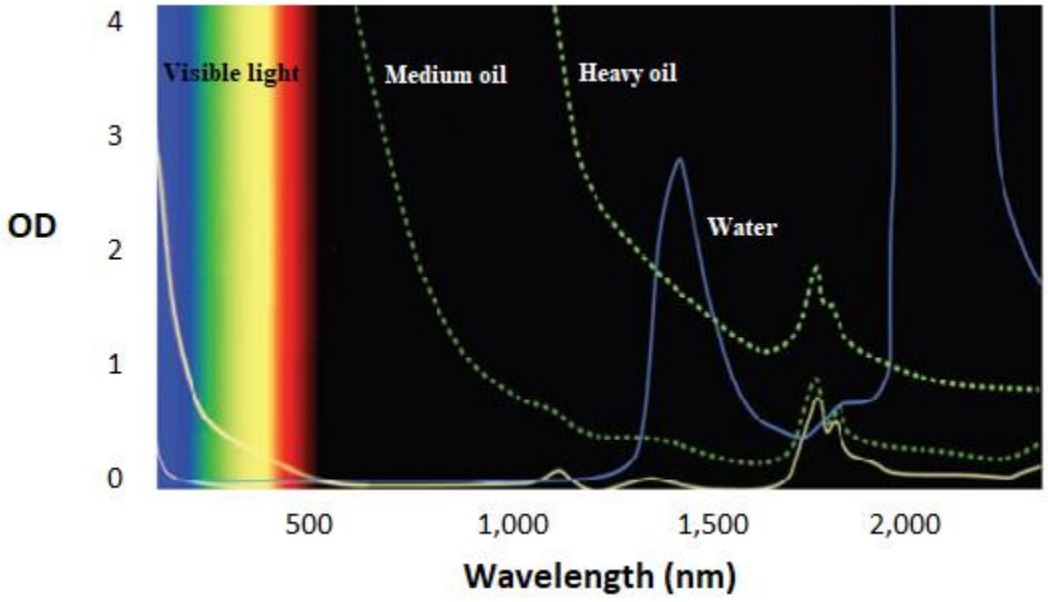

Figure 2: The optical density of crude oils in the visible and near-infrared spectra [44].

Refractometer based on measuring the critical angle technique has been used. The measurements were mostly attainable. However, this was not the case for some heavy crude oils. Therefore, the measurement had to be carried on several (crude oil/toluene) mixtures and the crude oil refractive index was calculated by extrapolating the data [45]. This method is simple, but it is time-consuming, and the measurement cannot be done in real time. Fiber optic sensor based on the intensity of the reflection signal has also been demonstrated, but the effect of the absorption continues when measuring heavy oils [46].

Fluorescent-core microcapillaries have also been used in the refractive index measurement of crude oil. This method gives a good result in the high refractive index range. However, the sensitivity, in the typical crude oil refractive index, was significantly low (22.9 nm/RIU) [47]. Finally, Surface Plasmon Resonance (SPR) sensor based on the Kretschmann configuration was presented [48]. This approach is based on varying the angle of incidence of a single wavelength laser and monitoring the intensity of the reflected light. This method has achieved high sensitivity, but the configuration used in this work requires mechanical components to control the movement of both the transmitter and the receiver. This adds a new challenge and makes the system not suitable for miniaturization. Different SPR techniques are available in more simplified ways. Kretschmann SPR sensor based on varying the wavelength is more practical since it does not need moving parts, but has somewhat less resolution [43]. Also, the plasmonic properties of gold nanoparticles deposited on a substrate can be used to measure refractive index, which is part of the scope of this thesis work.

2.2.3 SARA Analysis

One common technique to characterize crude oil is by fractionating it based on the solubility and polarity into saturates, aromatics, resins, and asphaltenes. This technique called SARA analysis. The process of SARA analysis is complicated and time-consuming; therefore, it is often skipped in the routine crude oil analysis [1]. The first step is removing the asphaltene from the crude oil by adding an n-alkane solvent such as heptane. Subsequently, the de-asphaltened oil is fractioned into saturates, aromatic, and resin by

chromatography methods. For each fraction, the solvent is removed by evaporation and then the fraction is weight [49]. Figure 3 shows a brief diagram of this approach.

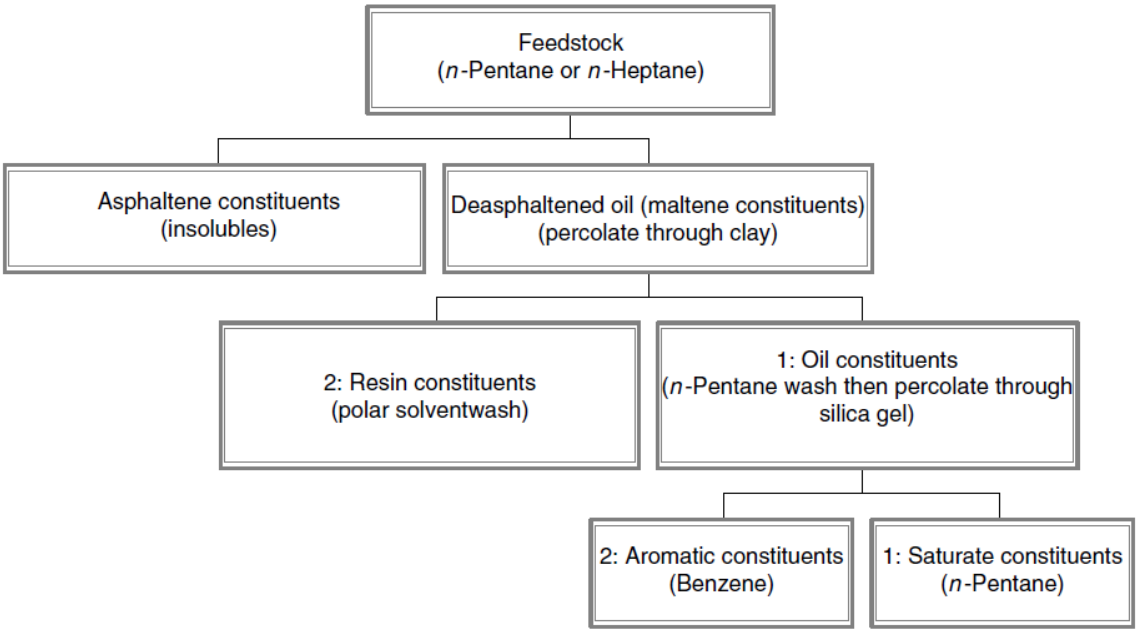

Figure 3: SARA fractionation procedure [1].

2.3 Crude Oils Asphaltene

Operations in the oil and gas industry are full of complexity, and the presence of asphaltenes is critical to different phases of the oil industry [1]. Asphaltenes are the heaviest, densest, and most polar component in the crude oil. They are a complex mixture of thousands of chemical components that have a deleterious effect on the production, transportation, and refining process. Because of their chemical and structural complexity, asphaltenes are defined by their high solubility in aromatic solvents (e.g., toluene) and low solubility in n-alkanes solvents (e.g., n-heptane). Asphaltene's tendency towards precipitation and deposition often causes serious problems for the wellbores and pipelines such as clogging and corrosion which reduce the oil flow and increase the non-production

time from maintenance [50-51]. To address these asphaltene related issues, researchers have investigated spectroscopic and analytical techniques for quantification and basic understanding [52].

The asphaltene is the most studied component of crude oil, and yet it is the least understood [52]. The elemental composition of asphaltene is probably the only information that is known and undebated. There has been a significant variation in the literature related to the asphaltene's molecular weight, but only recently most of the studies agreed that it is in the range of 500-1000 g/mol [53]. The molecular architecture of asphaltene is mainly polyaromatic hydrocarbons (PAH) with alkyl chains and heteroatoms such as S, O, and N. The number of PAH rings in asphaltene is believed to be seven, based on different imaging and spectroscopic techniques [54].

The aggregation and consecutively the deposition of asphaltenes can be triggered by a change in the crude oil pressure, temperature or composition. The mechanism of the aggregation process remains not completely resolved despite extensive research [54]. The modified Yen model which is also called "Yen-Mullins model" is the most recognized model for asphaltene aggregation (Figure 4). According to this model, the asphaltene exists as a single molecule of approximately 1.5 nm diameter. At a concentration higher than 100 mg/L, asphaltene molecules form nanoaggregates with an average of 6 molecules. These nanoaggregates can form what is called nanoaggregates clusters. There is uncertainty about the number of the nanoaggregates in one cluster, but it is estimated to be eight nanoaggregates [53]. To eliminate the costly consequences of asphaltene deposition,

researchers have been making tremendous efforts to understand asphaltene aggregation and its causes, but there are still questions not resolved [54].

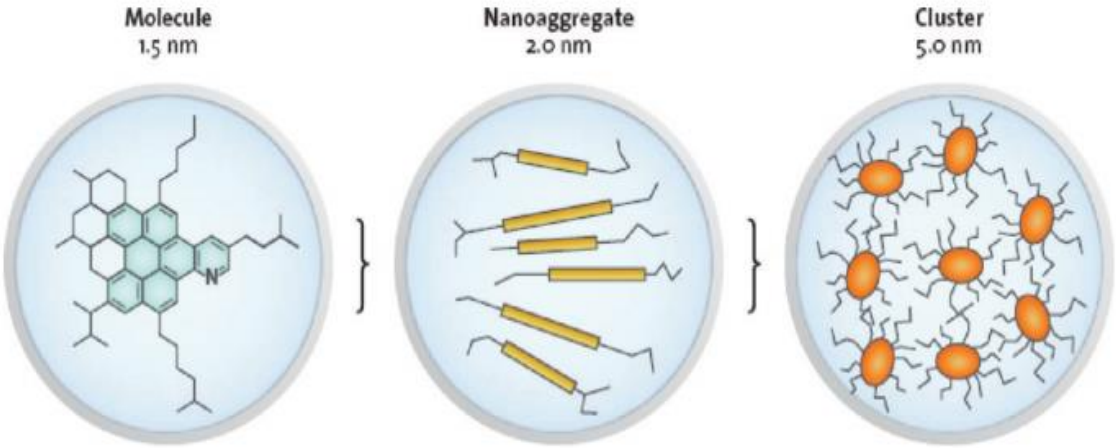

Figure 4: The Yen-Mullins model of asphaltene. Reprinted with permission from [53] Copyright © 2012, American Chemical Society.

Water is always co-produced with crude oil and even after the surface phase separation, traces of water still exist in the oil [1]. The interaction between asphaltene and water has been under wide research [55-58]. Calorimetric titration [55], and Fourier transform infrared spectroscopy [56] have shown evidence of this interaction. One work has suggested that water molecules could be trapped between asphaltene molecules [57]. Different work has suggested that H-bonding plays a key role in this interaction [56]. Other reports have observed the adsorption of water on asphaltene [51,58]. In all these reports, the mechanism of water-asphaltene interaction is not well understood or determined.

2.4 Characterization of Asphaltene

When it comes to the term ‘asphaltene characterization’, it is often referred to the information such as the asphaltene content in crude oil and the asphaltene yield curve measurement. This is at least from the industry point of view. These properties are explained in the following subsections.

2.4.1 Asphaltene Content Measurement

The measurement of the asphaltene content is an important parameter to determine the quality and properties of the oil. Therefore, an accurate and efficient method to determine the asphaltene content is important. There are few standardized methods reported in the past to measure asphaltenes [10-12]. They are gravimetric based methods that work by adding n-alkane to precipitate the solid particles, separate them by either filtration or centrifugation, and finally weigh the asphaltene using a balance scale. Even though this method is simple, it is time-consuming, requires a lot of solvents and a laboratory environment. The main disadvantage of this approach is the poor reproducibility that can show variations up to 20%, particularly from oils with low asphaltene (Table 2) [11].

Table 2: Standard deviation for Asphaltene measurement [11]

Asphaltene Content (%)	**Standard deviation (%)**
>3	10
1—3	20
<1	50

There have been numerous reports to address the gravimetric method issues using spectroscopic techniques. Part of these works aimed to measure the asphaltenes directly from the oil without extractions using techniques such as fluorescence spectroscopy [59], Fourier transform infrared [49], near-infrared [23], mid-infrared [24], all along with chemometric methods. On the other hand, another work has used a combination of separation and optical absorption efficiently to measure the asphaltene content [9]. In that work, it was shown that the asphaltene accounts for a great portion of the crude oil optical absorption in the visible and near-infrared range (Figure 5). The latter approach proved to be more accurate as it removes the uncertainty that comes from the analogous and interfering molecules to asphaltene such as resin.

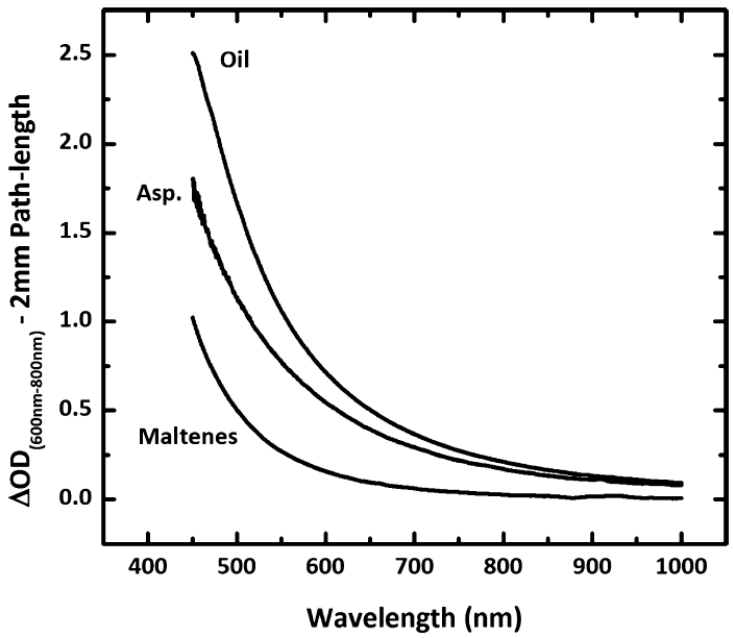

Figure 5: Optical spectra of diluted Oil, maltenes, and asphaltenes. Reprinted with permission from [9] Copyright © 2013, American Chemical Society.

2.4.2 Asphaltene Yield Curve Measurement

The measurement of the asphaltene yield curve is useful and contains an important information for the asphaltene phase behavior studies. The result of this measurement shows how much asphaltene precipitation due to gradual perturbation in its composition, generally by gradual addition of n-alkane. This helps in understanding the behavior of asphaltene in particular crude oil and possibly mitigate some costly problems. As it was mentioned above, the asphaltenes are defined based on their solubility. However, the asphaltene does not have a fixed solubility parameter but rather it has a range of solubility. Since the asphaltene is a mixture of molecules, some molecules have high solubility and they are the first to precipitate with small perturbation, and some molecules have lower solubility and they are harder to precipitate. The percentage of the asphaltene that would precipitate at each solvent/crude oil ratio is what one can observe in the asphaltene yield curve. Another important piece of information that can be extracted from this curve is the asphaltene precipitation onset point. This point is the ratio of the solvent/crude oil where the asphaltene starts to precipitate. Figure 6 shows asphaltene yield curve of different crude oils. Similarly, to the asphaltene content measurement, gravimetric based methods are the most standard approach to measure the asphaltene yield curve. But recently, researchers have reported using optical absorption, fluorescence spectroscopy and light scattering techniques to perform this measurement [60].

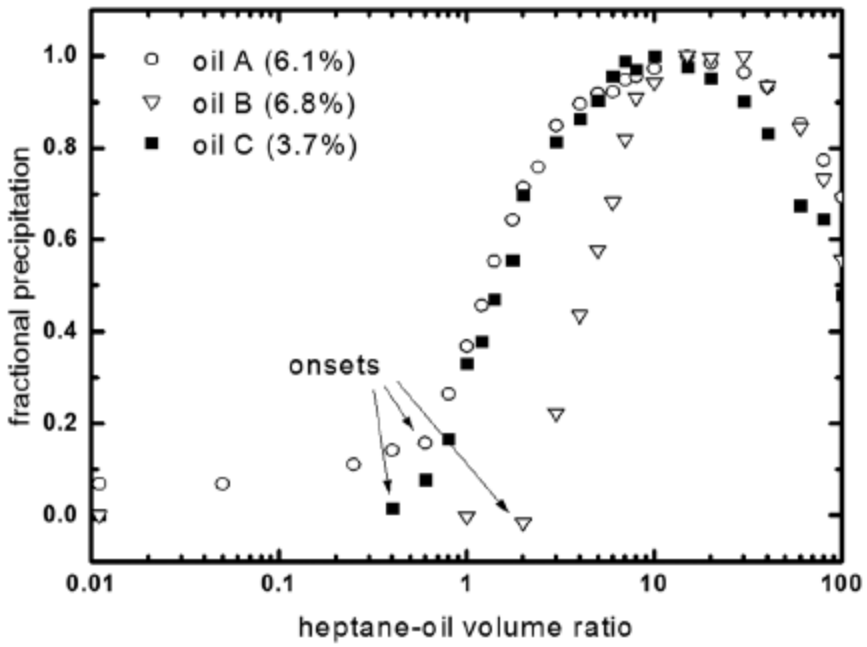

Figure 6: Asphaltene yield curves for three crude oils. Reproduced from Ref. [60] with permission from The Royal Society of Chemistry.

Chapter 3 Theory

3.1 Introduction

This chapter introduces the underlying theory of the methods used in this work. Section 3.2 talks about noble metal Nanoparticles (NPs). We explain the phenomena of localized surface plasmons resonance and discuss the effect of the size and shape of the NPs. The sensitivity of these NPs to the change of the surrounding refractive index is discussed. Finally, one of the key applications of NPs, which is Surface-Enhanced Raman Scattering (SERS) is explained.

Section 3.3 presents the basic principle behind the terahertz spectroscopy. This section briefly covers the different methods of THz generation and detection and gives details about a particular one, namely, Photoconductive Antennas (PCA) as this is the THz approach used in our work. In addition, the method of calculating the optical parameters such as refractive index and absorption coefficient is shown. Finally, we show the enhancement in the THz signals that can be accomplished by using plasmonic nanostructures.

3.2 Metal Nanoparticles

Gold NPs have gained high attention in a wide range of applications such as biomedicine [61], plasmon-enhanced spectroscopies [62], photovoltaics [63], and optical and optoelectronic devices [64]. When the frequency of the incident light overlaps with the nanoparticle free electron oscillation frequency, a strong absorption phenomenon occurs. This is known as Localized Surface Plasmon Resonance (LSPR) and it depends strongly on the shape and size of the particle, and the surrounding dielectric environment [6-7]. The LSPR peak is highly sensitive to the surrounding environment in a way that a red-shift occurs as the refractive index of the surrounding material increases [6]. Another feature of the nanoparticles is that they produce 'hot-spots' of large electric field enhancement which can magnify optical signals such as Raman and fluorescence. Surface-enhanced Raman spectrum is one of the key applications of nanoparticles [62]. These unique properties of nanoparticles have the potential to be used in a wide range of applications related to characterizing crude oil and its derivatives at different stages of the production and refining. To date, the plasmonic properties of metal nanoparticles have not been exploited.

3.2.1 Localized Surface Plasmon Resonance

When light interacts with a small particle, of size much smaller than the wavelength, of a material that has a negative real refractive index such as noble metals, an interesting phenomenon called localized surface plasmon resonance (LSPR) can be observed. As shown in Figure 7, the LSPR is a non-propagating surface plasmon confined at the surface of the particle when the oscillation of the free electrons matches the frequency of the light. This leads to significant field enhancement inside and outside the particle [65].

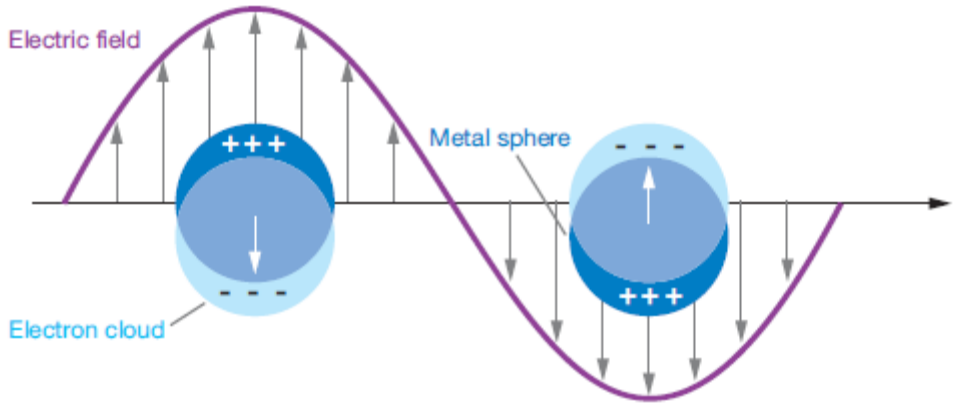

Figure 7: Schematic diagram of a localized surface plasmon [65].

One of the characteristics of NPs is their LSPR dependency on shape and size of the particle. This made it possible for NPs to be tuned so that they have LSPR at the desired frequency. Figure 8 shows extinction spectra of NPs with different shapes. The shape dependence of the LSPR is clear [6,66].

To understand more how the LSPR occurs, we can consider a small metal nanosphere in an electrical field (Figure 9). If the sphere diameter is much smaller than the light wavelength, the phase over the volume of the sphere can be assumed to be constant. In this case, the interaction can be electrostatic, and quasi-static approximation can be applied.

By solving the Laplace equation for the potential $\nabla^2\Phi = 0$, where Φ is the electrical potential, we can calculate the field by the gradient of potential $E = -\nabla\Phi$. The resulting field inside and outside the sphere are the following

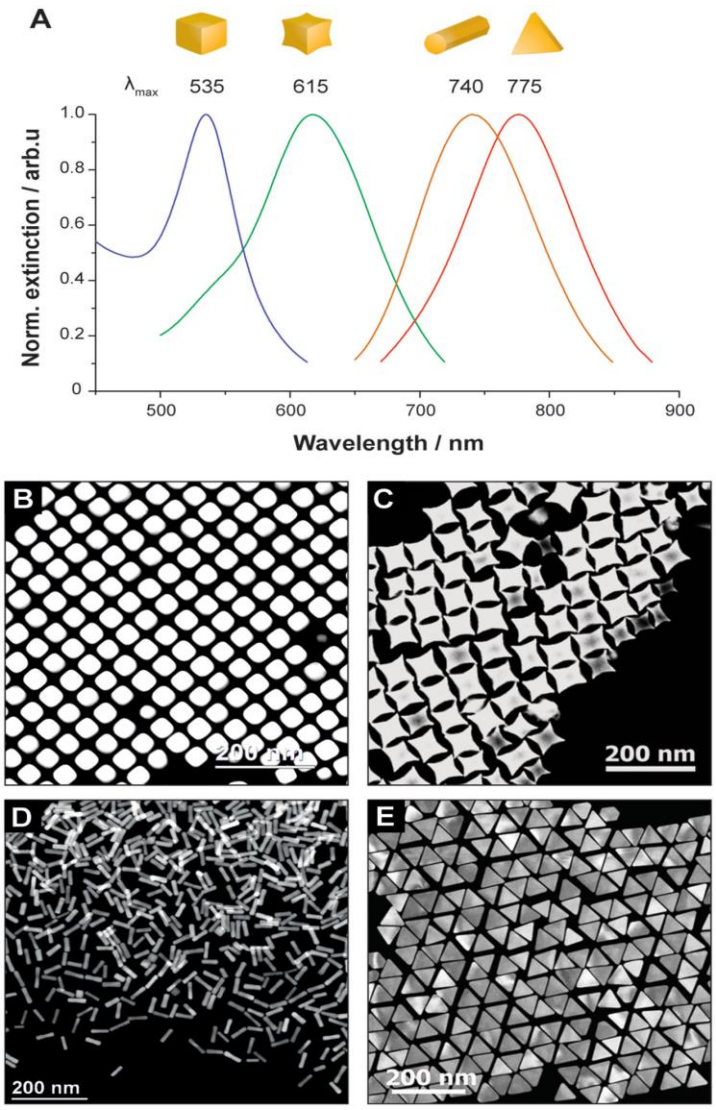

Figure 8: (A) Normalized extinction spectra and LSPR peak. (B—E) TEM images of nanocubes, concave nanocubes, nanorods, and nanoprisms [66].

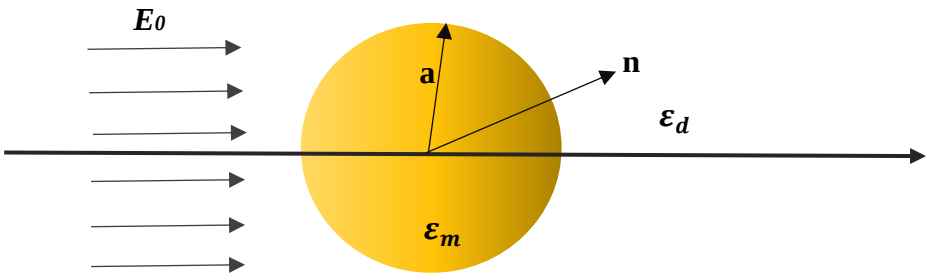

Figure 9: A metallic spherical nanoparticle of radius a in an electrostatic electric field.

$$E_{in} = \frac{3\,\varepsilon_m}{\varepsilon_m + 2\varepsilon_d} E_o \tag{2.1}$$

$$E_{out} = E_o + \frac{3\,n(n.p) - p}{4\pi\varepsilon_o \varepsilon_m\, r^3} \tag{2.2}$$

where $\boldsymbol{\varepsilon_m}$ is the permittivity of the sphere, $\boldsymbol{\varepsilon_d}$ is the permittivity of the surrounding medium, $\boldsymbol{\varepsilon_o}$ is the permittivity of the vacuum, **r** is the distance from the center of the sphere, $\mathbf{E_o}$ is the intensity of the incident field, **n** is a unit vector in the direction of observation, and **p** is the dipole moment which is given by

$$p = 4\pi\varepsilon_o \varepsilon_d a^3 \frac{\varepsilon_m - \varepsilon_d}{\varepsilon_m + 2\varepsilon_d} E_o \tag{2.3}$$

where $\boldsymbol{a}$ is the radius of the sphere. From (2.3), the polarizability α can be extracted via the relation $p = \varepsilon_0 \varepsilon_m \alpha E_0$ and we get

$$\alpha = 4\pi a^3 \frac{\varepsilon_m - \varepsilon_d}{\varepsilon_m + 2\varepsilon_d} \tag{2.4}$$

Since we have two materials with opposite sign permittivity, the denominator of the equations (2.1—2.4) can be zero in case of lossless material when $\varepsilon_m = -2\varepsilon_d$ and therefore the internal field and induced dipole moment will approach infinity. However, in reality, the metal has imaginary part in its permittivity and the dominator cannot be zero $|\boldsymbol{\varepsilon_d + 2\varepsilon_m}| \neq \mathbf{0}$ but this can give us a clear idea that when $|\varepsilon_d + 2\varepsilon_m|$ is minimum, there will be significant enhancement in the internal and external field [67].

Another interesting observation due to the LSPR resonance is its effect on the absorption and scattering of the nanospheres. The scattering and the absorption cross section are given by

$$C_{sca} = \frac{8\pi}{3} k^4 a^6 \left|\frac{\varepsilon_m - \varepsilon_d}{\varepsilon_m + 2\varepsilon_d}\right|^2 \quad (2.5)$$

$$C_{abs} = k4\pi a^3 Im \left[\frac{\varepsilon_m - \varepsilon_d}{\varepsilon_m + 2\varepsilon_d}\right] \quad (2.6)$$

where k is the wavevector in the surrounding medium, and Im indicates the imaginary part of the equation. From these Equations, we can see that both the scattering and absorption will exhibit a resonance when the term $|\boldsymbol{\varepsilon_d + 2\varepsilon_m}|$ is minimum. Also, it can be observed that the C_{sca} scales with a^6 whereas the C_{abs} scales with a^3. That means the extinction, which is the total of scattering and absorption, will be dominated by scattering in case of big particles and dominated by absorption in case of small particles [67].

3.2.2 LSPR Sensitivity to Refractive Index

The high sensitivity of NPs LSPR to the change of the surrounding refractive index has made them an appealing option for developing a chemical and biological sensing platform. As shown in Figure 10, the LSPR peak will exhibit a red-shift as the surrounding refractive index increases due to a material change or molecular adsorption on the surface. On the other hand, the LSPR peak can exhibit a blue-shift if the refractive index is decreased. This approach has shown high sensitivity and requires only a small amount of sample [68].

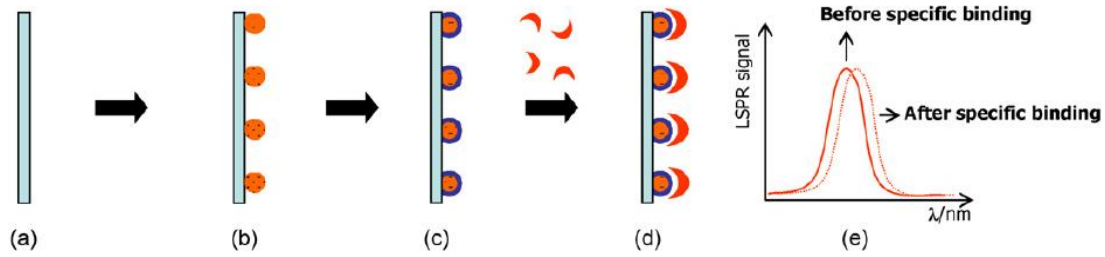

Figure 10: Preparation and response of LSPR sensor: (a) blank substrate, (b) NPs are immobilized on the substrate, (c) the NPs surface are functionalized with moiety, (d) analyte bound to the surface of the NPs, and (e) shift in the LSPR peak due to binding [68].

The refractive index sensitivity depends on the NPs shape, size, and LSPR peak position. In general, particles with sharper apexes will exhibit higher refractive index sensitivity. The refractive index sensitivity can be measured by dispersing the NPs in different fluids that have a different refractive index. A common way is to use a mixture of water/sucrose with linearly increased concentration. The sensitivity can be calculated by measuring the LSPR spectral shift ($\Delta\lambda_{max}$) that corresponds to the refractive index change. As shown in Figure 11, the nanorods and nanoprisms have the highest sensitivity [66].

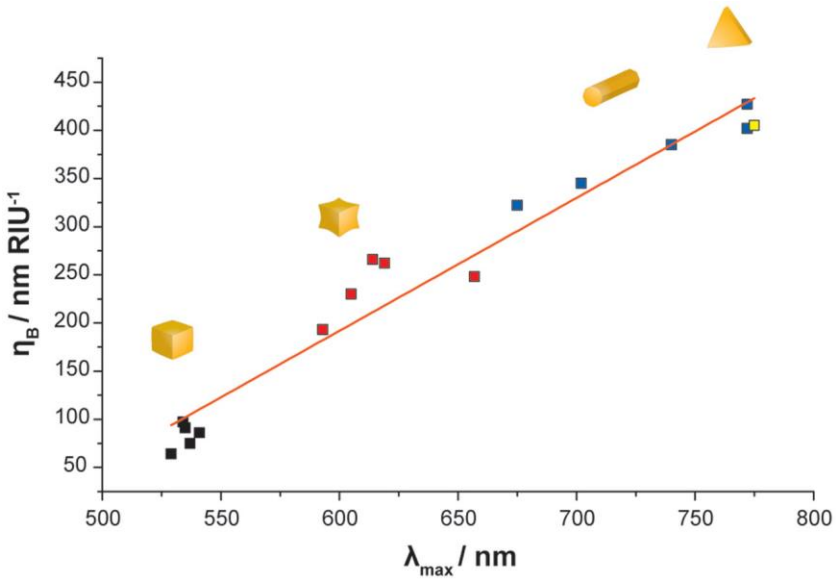

Figure 11: Bulk refractive index sensitivity for different NPs [66].

To realize a sensing platform using NPs, it is beneficial to immobilize the suspended particles in solution on a solid substrate. However, it has been shown that the sensitivity is considerably affected by that. When the NP is dispersed in solution, the whole surface is in contact with the fluid and therefore produces the maximum sensing capacity, whereas when the particle is immobilized on a substrate, a large portion of the sensing area will be

in contact with the substrate, reducing the effective total sensing area. The reduction in the sensitivity is proportional to the fraction of the area which is in contact with the substrate. Figure 12 shows a comparison between the refractive index sensitivity of NPs dispersed in solution and immobilized on a substrate. The reduction can be up to 36% in the case of nanorods [66].

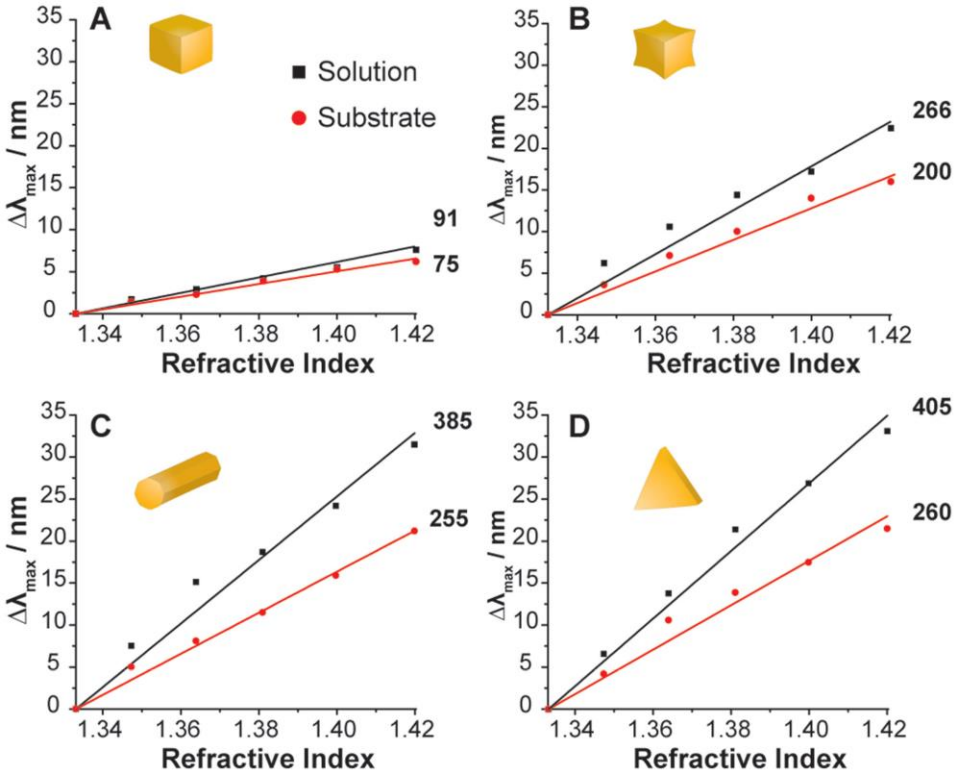

Figure 12: Comparison between the refractive index sensitivity of dispersed and immobilized (A) nanocubes, (B) concave nanocubes, (C) nanorods, and (D) nanoprisms [66]

The NPs are stabilized in solution with cetyltrimethylammonium bromide (CTAB). The CTAB forms a layer of approximately 3-4 nm. The electromagnetic waves decay rapidly from the NP surface in the perpendicular direction, which means the volume occupied by the CTAB is the largest part that can be sensed by the LSPR. Since this surfactant is not

needed when the NPs are immobilized on a substrate, removing the CTAB using plasma etching improves the sensitivity [66].

3.2.3 Surface-Enhanced Raman Scattering

To date, SERS is one of the main applications of NPs [8]. Before going into the details of SERS, we give a brief introduction about the Raman effect [69]. When monochromatic light is incident on a material, the vast majority of the photons will be scattered with the same energy level. This is called an elastic collision or Rayleigh scattering. On the other hand, a tiny portion of the photons will interact inelastically with the material and will be scattered with either lower energy (Stokes) or higher energy (anti-Stokes). Not every molecule is Raman active. A change in the polarization potential is required with respect to the vibration coordinate for Raman effect to take place. Each Raman active molecule has a unique Raman spectrum depending on the degrees of freedom of the molecules. Raman spectrum works as a fingerprint for molecules, therefore, Raman spectroscopy has found a wide range of applications in the fields of chemistry, physics, and biology.

Raman spectroscopy is represented by what is called a Raman shift, which has a wavenumber unit as it is related to energy. After recording the spectrum with a spectrometer, the Raman shift can be calculated by

$$\Delta\omega(cm^{-1}) = \left(\frac{1}{\lambda_0(nm)} - \frac{1}{\lambda_1(nm)}\right) \times \frac{(10^7 nm)}{(cm)} \tag{2.7}$$

where $\Delta\omega$ is the Raman shift in wavenumber with cm^{-1} unit, λ_0 is the excitation laser wavelength, and λ_1 is the Stokes wavelength. The factor 10^7 is to convert the wavenumber unit to cm^{-1}.

The main drawback of Raman spectroscopy is the intrinsic extreme weak process of Raman scattering. The typical Raman cross section is in the range of $10^{-28}\ to\ 10^{-24}\ cm^2$ per molecule making the detection of Raman spectrum hard or even impossible for some molecules without enhancement. SERS is the ultimate solution for this [70]. To get the highest SERS enhancement, it is required to tune the LSPR of the NPs to match the excitation laser wavelength or slightly red-shift the LSPR peak from the excitation wavelength so that the resonance covers both the excitation and the stokes wavelengths. By placing the molecule in the surface region of the NPs where the electric field of the excitation laser experiences a huge enhancement, the rate of the Raman scattering events will increase dramatically.

The SERS enhancement mechanism is due to two effects [70]: an electromagnetic (EM) effect, which is the essential part, and a chemical effect. The EM enhancement occurs due to the local field enhancement M_{Loc} and the radiation enhancement M_{Rad}. The M_{Loc} is the ratio between the field at the surface of the NP and the incident field. On the other hand, M_{Rad} is more complicated to define but it is often assumed to be equal to M_{Loc} resulting in estimation with an acceptable accuracy. Therefore, the SERS enhancement factor (EF) can be expressed by

$$EF \approx \frac{|E_{Loc}|^2}{|E_{Inc}|^2}\frac{|E_{Loc}|^2}{|E_{Inc}|^2} \approx \frac{|E_{Loc}|^4}{|E_{Inc}|^4} \tag{2.8}$$

Based on this equation, the SERS EF can be approximately estimated by the fourth power of the field enhancement.

SERS can be achieved through different approaches [70]. The simplest one is to mix the NPs solution with the analyte solution and then the measurement can be taken. This approach does not work well with an opaque solution. Alternately, the NPs solution can be deposited on a planar substrate, glass for example, and the analyte solution is dropped on the substrate. In these two approaches, the analyte molecules that fall in the vicinity of the NPs will experience a large SERS enhancement. As shown in Figure 13, the localized field can be further enhanced compared to what we get from a single NP when two NPs become close to each other, forming a gigantic electric field region that is often called a 'hot-spot' resulting in a higher SERS enhancement [71].

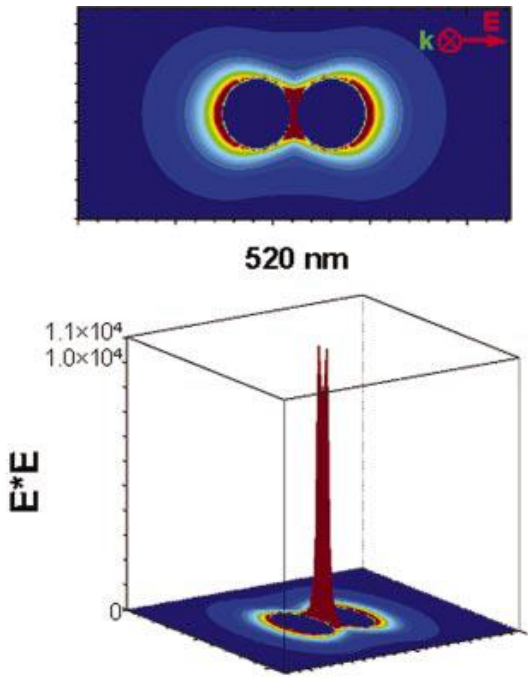

Figure 13: E-field enhancement of a dimer of Ag nanoparticles separated by 2 nm. In the 3D plots, the axis perpendicular to the selected plane represents the amount of E-field enhancement around the dimer [71].

The typical SERS enhancement by colloidal NPs or NPs dispersed on a substrate is in the range of $10^6 - 10^7$ whereas SERS enhancement in case of a few nanometers gap can be up to 10^{14} [72]. Figure 14 shows an example where normal Raman measurement does not show any peak, SERS from NPs shows a small feature, and SERS from molecules in the gap of adjacent NPs shows the strongest Raman spectra [73].

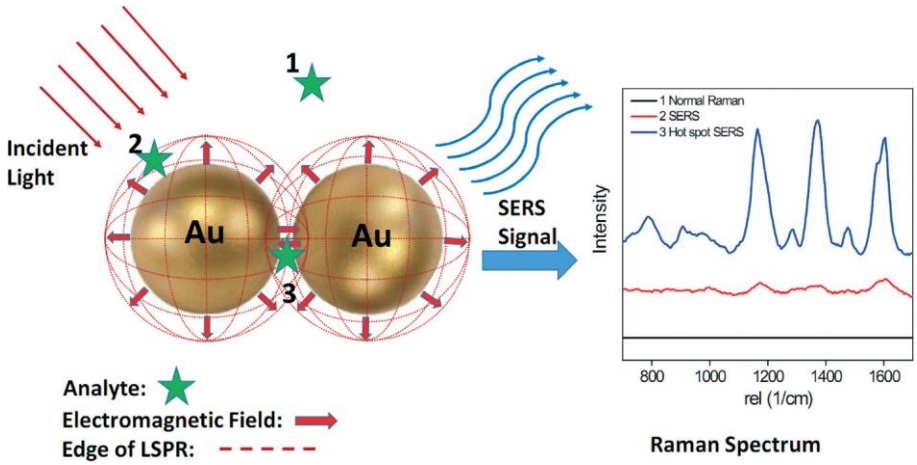

Figure 14: Schematic of SERS phenomenon for an organic analyte on a different position with respect to NPs. [73] Published by The Royal Society of Chemistry.

3.3 Terahertz Spectroscopy

The Terahertz (THz) region of the electromagnetic spectrum, which is in the frequency range of 0.1—20 THz and corresponds to photon energies of millielectronvolt (meV), has remained unexploited for a long time. These THz frequencies fall between the infrared and microwave range and as a result, it was challenging for both the electronic circuits to reach the THz lower edge and the optical sources to reach THz upper edge. Hence, it is often

called ‘terahertz gap’. The interactions between THz radiation with this low photon energy and matter can reveal valuable information to scientists and engineers such as unique fingerprints of materials, carrier dynamics in electronic materials, and rotational and vibrational transitions in molecules. In addition, some materials that are opaque in the visible range are transparent or exhibit low absorption in THz range, which makes it possible to study them using THz spectroscopy [17-19]. Examples of what can be studied by THz spectroscopy are shown in Figure 15

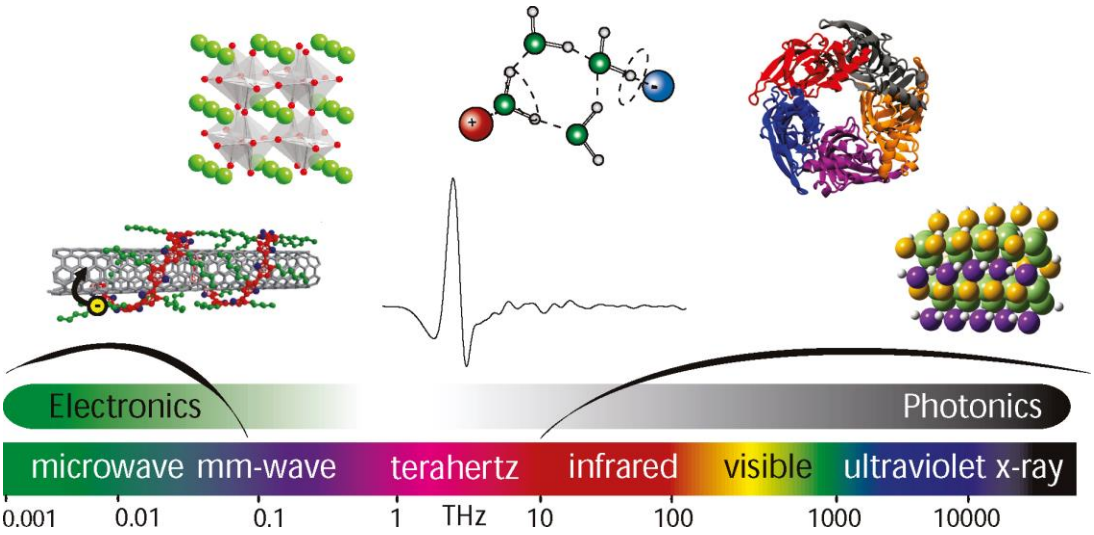

Figure 15: THz frequency in the electromagnetic spectrum with images of a variety of molecules, materials, and phenomena that can be studied by THz spectroscopy. Reprinted with permission from [17] Copyright © 2011, American Chemical Society.

3.3.1 Generation and Detection of THz Signals

There are a few established techniques for generation and detection of THz signals. The most common one is known as Time-Domain THz Spectroscopy (THz-TDS) which will be covered in detail in this section. Other techniques include using continuous wave and nonlinear properties of materials for THz generation will be presented briefly.

3.3.1.1 Photoconductive Materials THz-TDS.

THz-TDS measurement is based on a pump and probe operation. Femtosecond (fs) pulses are split by a beam splitter into a pump beam and a probe beam. The pump beam is focused on the Photoconductive Antenna (PCA) for THz generation, whereas the probe beam is focused on a different PCA for detection. The THz radiation travels through the sample under test which affects its amplitude and phase simultaneously. For the THz radiation to be detected, the optical pulses and the THz signal must arrive at the receiver PCA at the same time. Therefore, a mechanical delay line is used to change the optical length of the probe beam. The current is measured by a lock-in amplifier and Fourier transform is applied over the acquisition period in order to get its spectrum. A typical THz-TDS system is shown in Figure 16 [19].

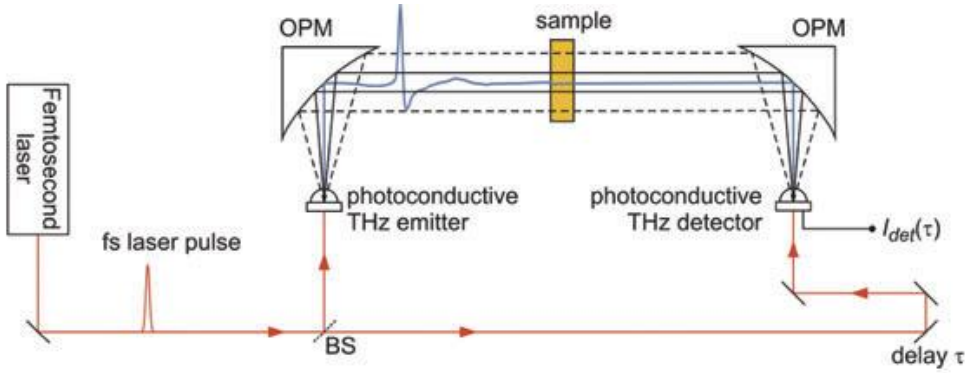

Figure 16: THz-TDS using PCA antenna schematic diagram [19].

The PCA antenna is the key component in THz-TDS system. As shown in Figure 17, the PCA consists of a substrate made of a semiconductor material and two metal electrodes connected to an antenna (e.g. a dipole). The PCA works as a switch that becomes conductive when exposed to light and becomes an insulator when the light disappears. When the light energy is greater than the band gap of the semiconductor material, the

photons will be absorbed and free carriers, electrons and holes, are generated making the PCA switch to a conduction state [74].

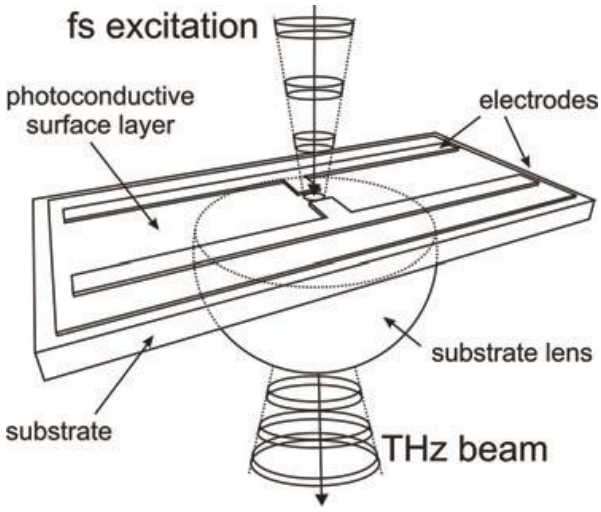

Figure 17: Photoconductive antenna for generation of ultrashort THz transients that are collimated into a free-space beam by a substrate lens attached to the antenna structure [19].

To generate a THz radiation, the PCA electrodes are biased with a DC voltage and the light is focused at the gap region of the antenna. The free carriers which were generated by the light will be driven under the effect of the biasing field, generating a photocurrent flows between the antenna arms. This photocurrent is a time-varying current that radiates electromagnetic waves with frequency components in the THz range. By ignoring the contribution of the holes, since their mobility is much smaller than electrons, the photocurrent density can be expressed by

$$J(t) = N(t)q\mu E_b \tag{2.9}$$

where N is the photocarriers density, q is the charge of the electron, μ is the mobility of the electron, and E_b is the biasing electric field.

The radiated far-field electric field is proportional to the derivative of the generated photocurrent

$$E_{(r,t)} = \frac{l}{4\pi\varepsilon c^2}\frac{di(t)}{dt}\ sin\theta \qquad (2.10)$$

where L is the dipole length, θ is the angle from the surface normal of the antenna, ε is the dielectric constant of the medium, and *c* is the speed of light in vacuum. To get a strong THz radiation, large current transition at sub-picoseconds is essential. And to get a large current transition, it is required to use high biasing field with strong laser pulse. On the other hand, high mobility is required to get a sharp overshoot and a broader THz bandwidth.

On the detection side, the same PCA can be used with a slight difference in the connections. The PCA does not need to be biased in this case because the THz electric field will induce a transient biasing voltage across the gap that will drive the free carriers to the electrodes. The electrodes, in this case, are connected to a lock-in amplifier which can measure small current accurately. To get an electromagnetic radiation or detection in the THz region, the switching time must be in the sub-picosecond time. The desirable properties to have a fast switching material are a short carrier lifetime and a high carrier mobility, in addition to having short fs laser pulse. Several semiconductor materials have been explored for THz application, the most common one is probably LT-GaAs due to its low fabrication cost, high mobility, and controllable lifetime [19,74].

In addition to the substrate material, the PCA antenna plays a crucial role in the amplitude and bandwidth of the detected THz signal. Dipole and bowtie (Figure 18) are common antennas in THz-TDS spectroscopy. Typically, bowtie antennas exhibit a stronger field

amplitude than dipole antenna, but the radiation has a narrower bandwidth. Dipole antenna geometry (dipole length, width, and gap size) can be tuned to have certain antenna specification. For example, as the length of the dipole decreases, the frequency of the maximum current response increases. Also, as the gap between the dipole arms decreases, the bandwidth of the detected THz radiation increases. However, this comes at the cost of having less THz amplitude as less electric field couples to the antenna. Therefore, a reasonable tradeoff between the amplitude and bandwidth can be achieved by having a dipole length of 20~30 μm and a gap length of~5 μm [75].

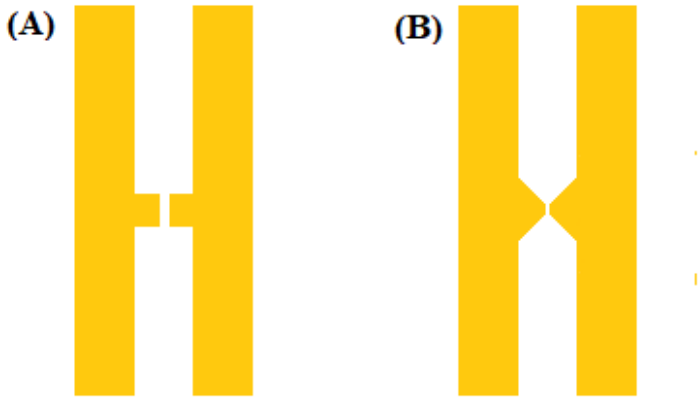

Figure 18: Schematic of the two most common THz antennas. (A) is a dipole antenna, (B) bowtie antenna.

The THz radiation is weak, and the directivity of the dipole is not sufficient to focus the field at the receiver antenna. In addition, the high dielectric constant contrast between the substrate (e.g. $\varepsilon_r = 12.9$ in GaAs) and the air, ($\varepsilon_r = 1$), forces the majority of light to be transmitted into the air but to refract away more from the normal, compared to the incident angle. Therefore, a mechanism for collimating or focusing the THz radiation is needed. As shown in Figure 17, silicon lens is used to solve this issue by attaching it to the back side of the PCA. It is made of highly resistive silicon so that its refractive index can be matched

to the PCA substrate. Figure 19 shows that the dimensions and geometry of the lens can be designed in a way that makes it collimates, diverges, or focuses the THz radiation. Collimating and focusing lenses are suitable for line of sight alignment but they are harder to align, whereas the diverging lenses need extra parabolic mirrors to collimate the beam, but in general, they are easier to work with [76-77].

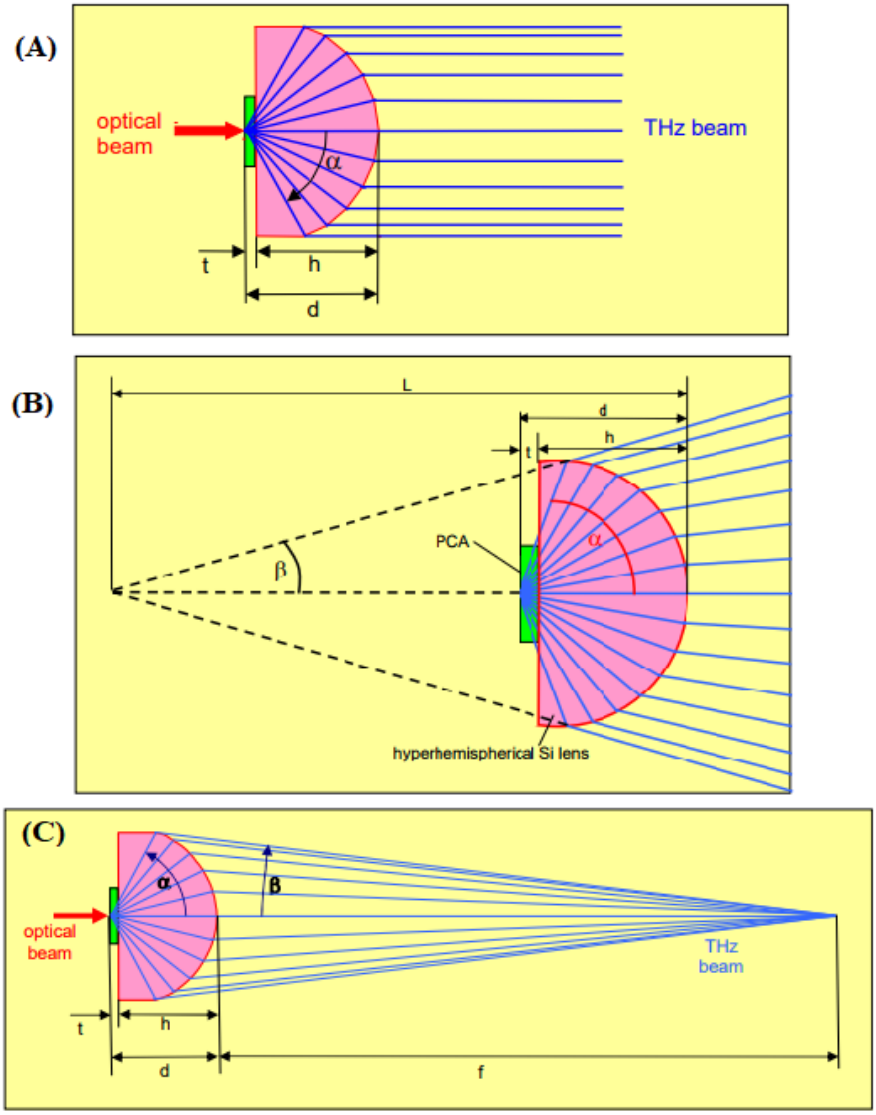

Figure 19: THz radiation pattern due to different silicon lenses. h is the lens height, α is the collection angle, and β is the divergence angle. (A) is a collimating lens, (B) is a divergence lens, and (C) is a focusing lens. Adopted from www.batop.com

3.3.1.2 Optical Rectification THz-TDS

In this method, an intense pulsed laser is used to excite a non-linear medium and to make the electrons oscillate. The term ‘non-linear medium’ refers to any material that has a non-linear relation between their polarization density (P) and electric field (E). The generation depends on a difference-frequency mixing of the frequency components of the optical pulse. When a femtosecond laser pulse incident on a non-linear crystal, it generates a time-varying polarization of dipoles in the crystal. Consequently, a transient electric field that fits the intensity envelope of the optical pulse is generated, thus, it is called an optical rectification. The generated electric field has frequencies in the THz region and travels with the laser beam.

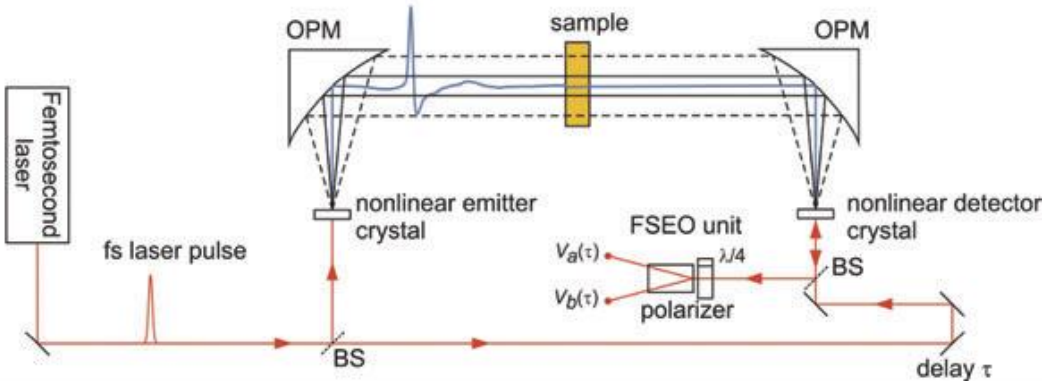

Figure 20: Schematic diagram of THz-TDS using an optical rectification [19].

On the detection side, an opposite process of the optical rectification technique is used, which is called electro-optical sampling. In this technique, both the THz radiation and the probe beam travel through the crystal and the THz field is measured by modulating the phase of the probe beam. When the THz field goes through the crystal, it induces a polarization change and therefore a change in the refractive index of the crystal. This

change will modulate the phase of the linearly polarized optical probe beam which can be measured by splitting the optical beam into its two orthogonal components by a series of a quarter-wave plate, Wollaston beam splitter, and two photodetectors for measuring the difference. A typical THz-TDS system using optical rectification is shown in Figure 20 [19,78].

3.3.1.3 Continuous-Wave THz-FDS.

This method is based on modulating the conductivity of the photoconductive material by a continuous wave with a frequency in the THz region. This can be achieved by using two monochrome lasers and by carefully choosing their wavelengths, the beating frequency can be tuned in the THz range. The two lasers are linearly polarized with the same polarization angle and propagate together toward the semiconductor photomixer. When the photomixer is biased, a photocurrent will be generated and modulated by the THz beating frequency. This photocurrent generates a narrow band continuous-wave (CW) THz radiation, which can be coupled to air by an antenna and a silicon lens, in a similar way to the PCA used in THz-TDS but with different antenna design consideration.

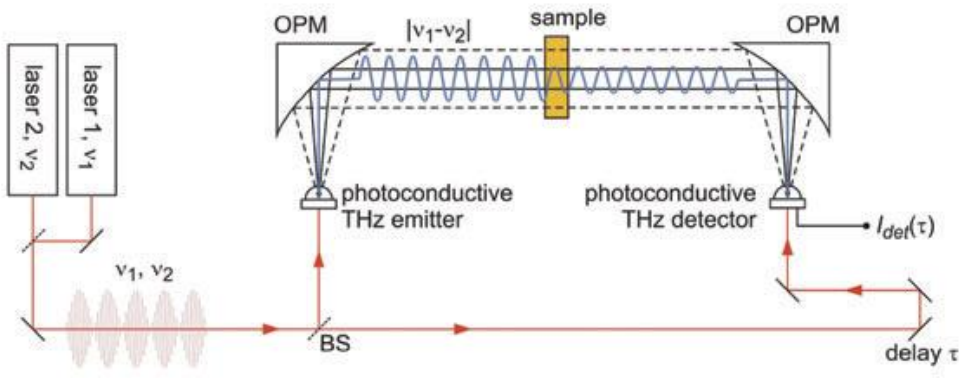

Figure 21: Schematic diagram of THz-FDS using a continuous wave [19].

The detection of CW THz radiation is the inverse process of its generation. The same photomixer is used without biasing and the measured photocurrent can be expressed as the product of the instantaneously conductivity, which is driven by the incident lasers and the THz field incident on the photomixer [19,79]. A typical THz-FDS system using CW is shown in Figure 21 [19].

3.3.2 Optical Parameters Calculation

THz-TDS is a technique often used in measuring the complex refractive index ($\hat{n} = n + i\kappa$) of the material under test, where n is the real refractive index and κ is the extinction coefficient. However, what the THz system is physically measuring is the temporal response of the THz electric field that is traveling through the sample. The optical parameters are calculated indirectly by comparing a reference THz pulse with a THz pulse travelling through the sample. The reference measurement can be taken either in air or in some conditions in nitrogen or vacuum, depending on whether or not it is sensitive to absorption of the ambient air. The sample will induce a change in the THz pulse amplitude, shape, and time delay. From these changes, the complex refractive index can be extracted. Since the measured pulse is in the time domain, the first step is to take a Fourier transform for the time domain raw data and by comparing the reference and sample spectrum, the optical parameters can be calculated in the frequency domain [19].

If we consider an electromagnetic plane wave propagating through a sample, we can express its time-dependent electric field as

$$E(z,t) = E_o \exp\left[i(\omega t + \frac{\hat{n}\omega}{c} z)\right]$$

$$E(z,t) = E_o \exp\left[i(\omega t + \frac{n\omega}{c}z + \frac{i\kappa\omega}{c}z)\right]$$

$$E(z,t) = E_o(t)\exp\left(i\frac{n\omega}{c}z\right)\exp\left(-\frac{\kappa\omega}{c}z\right) \quad (2.11)$$

where $E_o(t) = E_o e^{-i\omega t}$ is the time varying component of the electric field, ω is the angular frequency of the field. The first exponential term in Eq. 2.11 is the phase due to wave propagation and the second exponential term is due to medium absorption.

To calculate the optical parameters in the frequency domain, we can take the Fourier transform of the Eq. 2.11

$$E(\omega) = E_o(\omega)\exp\left(i\frac{n_{(\omega)}\omega}{c}z\right)\exp\left(-\frac{\kappa_{(\omega)}\omega}{c}z\right) \quad (2.12)$$

Now if we consider that we have a sample (Figure 22) of thickness *d* that we need to calculate its complex refractive index, we can express the electric field that has propagated through it by Eq. 2.12 as

$$E_{sample}(\omega) = E_{o(\omega)}\,T_{(\omega)}\exp\left(i\frac{n_{(\omega)}\omega}{c}d\right)\exp\left(-\frac{\kappa_{(\omega)}\omega}{c}d\right) \quad (2.13)$$

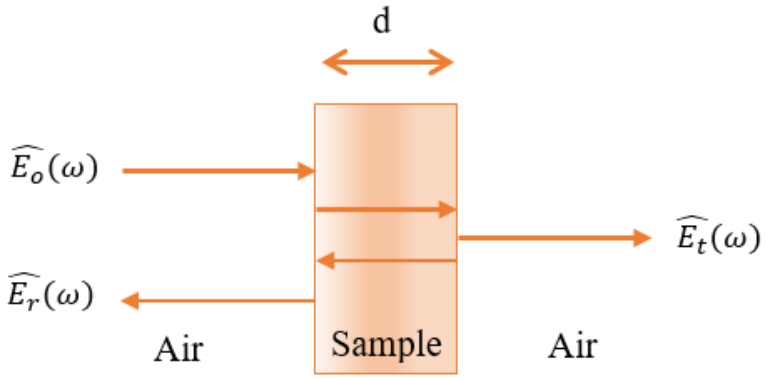

Figure 22: Diagram of THz pulse propagation through a sample of thickness d. Part of the incident wave is transmitted and part is reflected.

where $T_{(\omega)}$ is the transmission coefficient. When an electromagnetic wave propagates from one medium that has a refractive index n_1 to another medium that has a refractive index n_2, some loss occurs due to the reflection at the interface. This loss increases as the variation between the two indexes increases and can be calculated according to Fresnel's equations by

$$T_{12} = \frac{2n_1}{n_1+n_2} \tag{2.14}$$

In the case of the sample shown in Figure 22, there are two interfaces that cause losses in the transmission (air→sample and sample→ air). The transmission coefficient in Eq. 2.13 is the product of transmissions of the two interfaces. By taking ($n_1 = 1$) for air we get

$$T_{(\omega)} = T_{12} * T_{21} = \frac{4n_2}{(1+n_2)^2} \tag{2.15}$$

Equation 2.12 can be used to express the reference electric field pulse in air by substituting the parameters ($n = 1, \kappa = 0$), which gives

$$E_{reference}(\omega) = E_{o(\omega)} \exp\left(i\frac{\omega}{c}d\right) \tag{2.16}$$

The transfer function of the system can be given by dividing Eq. 2.13 by Eq. 2.16

$$H_{(\omega)} = Ae^{i\phi} = \frac{E_{sample}(\omega)}{E_{reference}(\omega)} = \frac{4n_2}{(1+n_2)^2} * \exp\left(i\frac{(n_{(\omega)}-1)\omega d}{c}\right)\exp\left(-\frac{\kappa_{(\omega)}\omega d}{c}\right) \tag{2.17}$$

Since A is the Fourier transform amplitude ratio between the sample and the reference, and ϕ is the phase difference between the sample and the reference, the refractive index and the extinction coefficient can be extracted from Eq. 2.17 as

$$n_{(\omega)} = 1 + \frac{\phi c}{\omega d} \tag{2.18}$$

$$\kappa_{(\omega)} = -\frac{c}{\omega d}\, ln\left[\frac{(1+n_2)^2}{4n} * A\right] \tag{2.19}$$

The absorption coefficient $\alpha_{(\omega)}$ is related to the extinction coefficient $\kappa_{(\omega)}$ by

$$\alpha_{(\omega)} = \frac{2\kappa_{(\omega)}\omega}{c} = -\frac{2}{d}\, ln\left[\frac{(1+n_2)^2}{4n} * A\right] \quad (2.20)$$

Eq. 2.18 and 2.20 are the ones used to calculate the optical parameters in the THz region. In general, they give accurate results. The basis for this analysis is the fact that the sample is a bare slab in the air, which is applicable only for solids. In spectroscopy, it is often required to characterize fluids or powders that need to be put in solution. Therefore, the material needs to be contained in a cell for the measurement to take place (Figure 23).

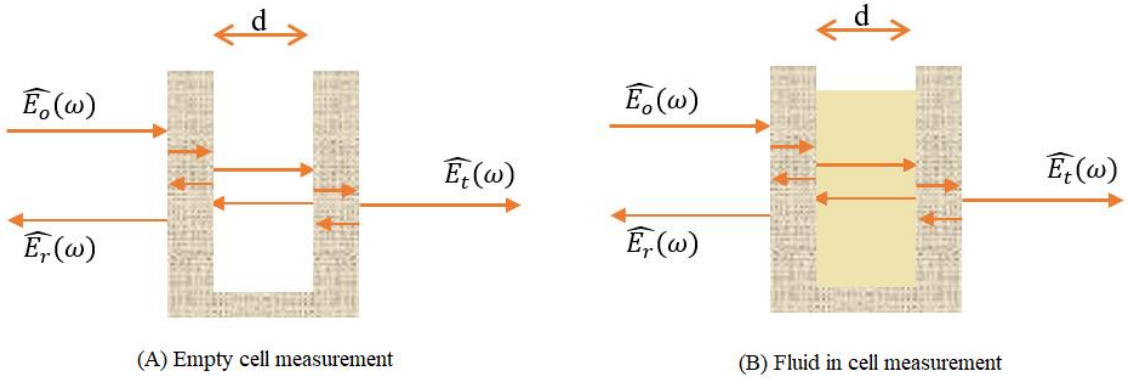

Figure 23: Schematic diagram of the reference and the sample measurements show the THz propagations and reflections along different interfaces.

In this case, the transmission coefficient $T_{(\omega)}$ is not the same as the one calculated by Eq. 2.15. This is because here we have four different interfaces. The transmission coefficient through the cell can be expressed by

$$T_{cell(\omega)} = T_{ac} * T_{cs} * T_{sc} * T_{ca} \quad (2.21)$$

where the letters *a*, *c*, and *s* refer to air, cell, and sample respectively. The measurement of the refractive index is not affected by this change since Eq. 2.18 is not dependent on the transmission coefficient, but it does affect the absorption coefficient. However, the Eq. 2.19 is still being used widely as the cell material often chosen out of materials that have a

low absorption and a small refractive index in the THz range. In addition, the reference measurement is taken with the empty cell so by normalizing the sample measurement by the reference measurement, most of the cell effect will be eliminated.

3.3.3 Plasmonic-Enhanced THz

PCA antennas exhibit limited low optical to terahertz conversion efficiency and therefore low THz radiation. This has encouraged researchers to look for ways to enhance the light coupling to semiconductor materials. Plasmonic enhancement has shown promising results in this subject. Before going into some details of the plasmonic enhanced THz generation and detection, we give a brief introduction about the underlying theory of this phenomena.

3.3.3.1 Surface Plasmon Polaritons

One type of surface plasmons, namely LSPR, was covered in detail in section 3.2.1. The other one is called surface plasmon polaritons (SPPs) and is found in more applications in the THz work. Unlike LSPR which occurs on a closed surface, SPPs is propagating waves at a planar interface between a metal and a dielectric and decay evanescently in the transverse direction in both directions (Figure 24). On the other hand, both LSPR and SPP are generated due to a different sign in the dielectric function and both produce a significant field enhancement.

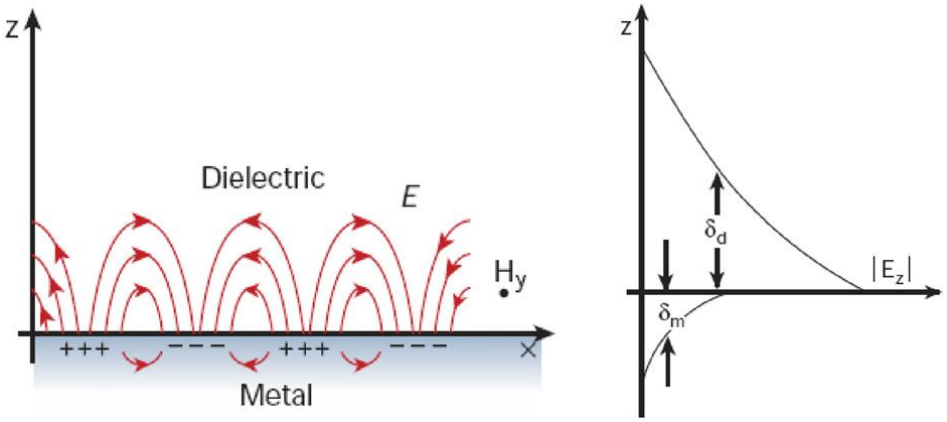

Figure 24: (Left) schematic illustration of SPP waves propagating at the interface between a metal and a dielectric material. (Right) shows the enhancement of the evanescent field near the surface and exponentially decaying in the transverse direction [80].

By using Maxwell's equations and applying the boundary condition, only transverse magnetic (TM) mode exists with a propagation constant

$$k_{spp} = k_x = k_0 \sqrt{\frac{\varepsilon_m \varepsilon_d}{(\varepsilon_m + \varepsilon_d)}} \tag{2.22}$$

where k_0 is the free space wavevector, ε_m and ε_d are the dielectric constants of the metal and the dielectric medium. Note that k_{spp} tends to be infinite, in case of lossless materials, when the condition $|\varepsilon_m + \varepsilon_d| = 0$ is satisfied producing a large evanescent field at the surface. The frequency when the SPP is maximum can be calculated. The dielectric constant of metal has the form

$$\varepsilon_m = 1 - \frac{\omega_p^2}{\omega^2} \tag{2.23}$$

where ω_p is the metal plasma frequency. Since the maximum SPP occur when $\varepsilon_m = -\varepsilon_d$, we can substitute ε_m in Eq. 2.23 with $-\varepsilon_d$ and the SPP frequency can be found as

$$\omega_{spp} = \frac{\omega_p}{\sqrt{1+\varepsilon_d}} \tag{2.24}$$

By using Eq. 2.22 and 2.23, the SPP dispersion relation can be plotted. Figure 25 shows the SPP dispersion curve of the gold-air interface compared with the free space wavevector. A nonlinear trend can be seen in the SPP dispersion and the k_{spp} increases exponentially as the frequency ω approaches the SPPs frequency ω_{spp}. This shows a momentum mismatch between the SPP waves ($\hbar k_{SPP}$) and the light in free space ($\hbar k_0$), which means special techniques to couple the incident light with the SPPs waves are required. The momentum of light can be matched with SPP momentum using prism couplers, grating structures, and waveguide couplers. Figure 26 shows schematic diagrams of these techniques [80].

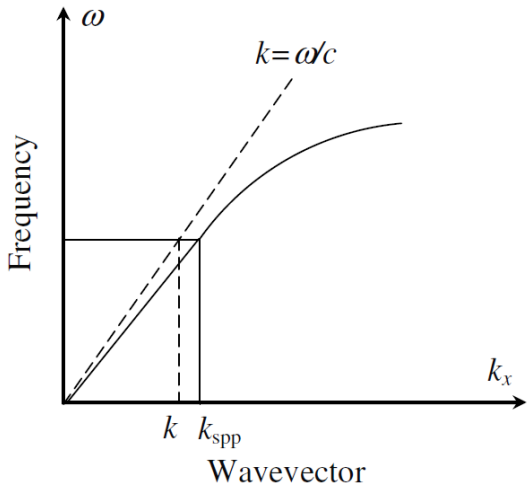

Figure 25: Dispersion curve of SPP (solid line) at a metal-dielectric interface compared with free space (dashed line) wavevectors [80].

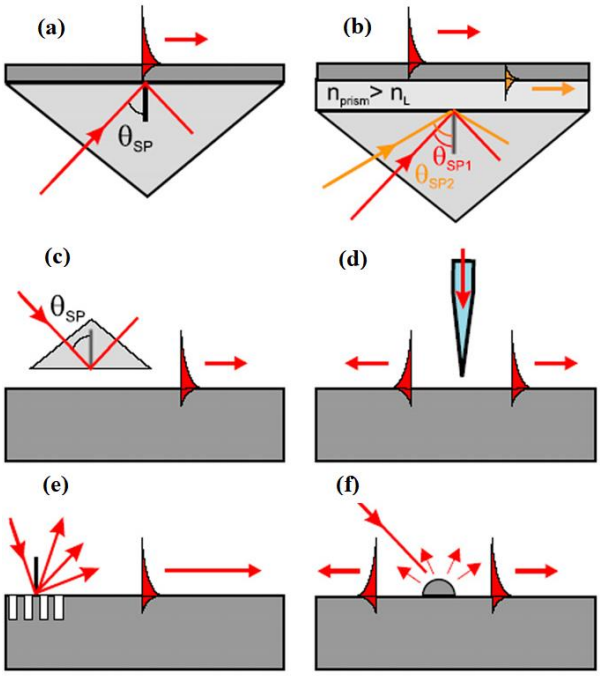

Figure 26: Different configuration for SPP excitation: (a) Kretschmann geometry, (b)two-layer Kretschmann geometry, (c) Otto geometry, (d) scanning near-field optical microscope probe, (e) grating structure, and (f) a diffraction on surface structure [80].

3.3.3.2 Examples of Plasmonic-Enhanced THz

Most of the induced photocurrent that radiates electric field in the THz range is generated from carriers very close to the antenna electrodes. This is because the carriers that arrive at the electrodes within sub picoseconds with approximately 10^7 cm/s velocity are arriving from within only few hundred nanometers. The other carriers either recombine for short carrier lifetime materials or contribute to the DC current [81]. Therefore, fabricating an antenna with a small gap seems beneficial, but the diffraction limit is another challenge when making small structures. Different plasmonic structures have been proposed to overcome this limitation. Plasmonic contact electrodes (Figure 27) have been shown to enhance THz radiated power by 50 times compared to non-plasmonic PCA. By designing

a proper plasmonic structure for the electrodes, a significant amount of light can be coupled to the substrate while using structures in the hundred-nanometer scale, and the diffraction limit can be overcome. In addition, these structures have reduced significantly the travel path for the generated free carriers, thus, it is possible to not use short-carrier lifetime semiconductors for THz operation [81].

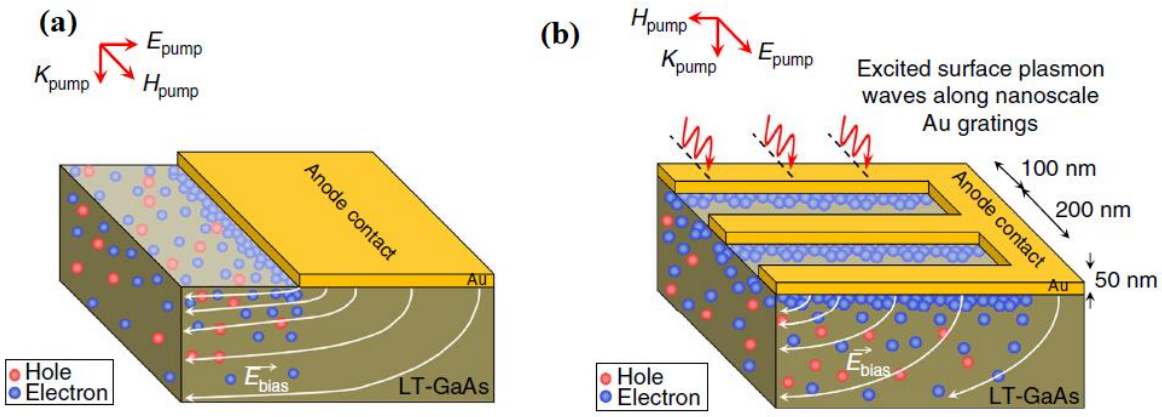

Figure 27: (a) Anode of PCA antenna with bias voltage is applied which induces an electric field drifts the free carriers towards the electrodes. (b) A PCA with plasmonic contact electrodes to enhance the THz generation and detection [81].

In a different work, a plasmonic enhancement made it possible to use LT-GaAs in THz generation and detection by a 1.5 µm femtosecond laser. Sources and detectors using this wavelength are desirable compared to 800 nm lasers as the laser technology is mature, has lower cost, more compact, and can be coupled with a fiber. In addition, LT-GaAs is several times cheaper than InGaAs, which is commonly used for 1.5 µm wavelength lasers. By using a simple plasmonic structure of slit array it was possible to generate a THz signal that significantly outperforms the commercial InGaAs devices in terms of power and bandwidth using 1.5 µm wavelength lasers. Figure 28 shows an SEM image of the structure

and a simulation for its field enhancement. This field enhancement is a key for the below band gap absorption in LT-GaAs when using 1.5 µm laser [82].

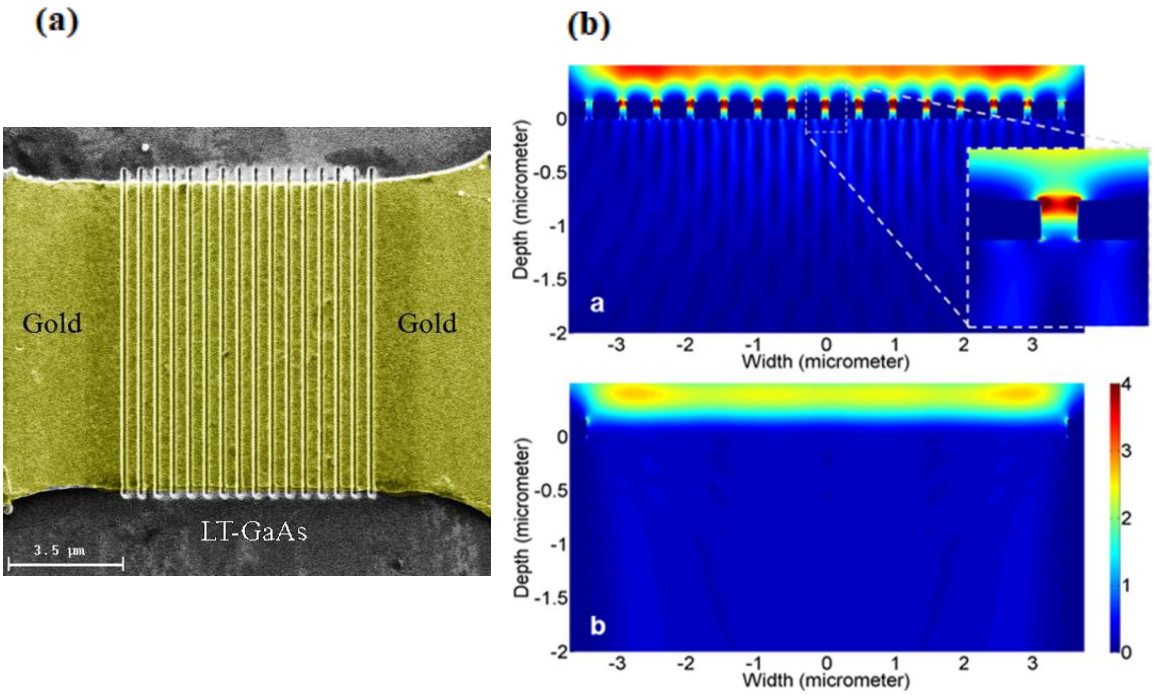

Figure 28: (a) Scanning electron microscope (SEM) image of a slit array with 100 nm gap size and 490 nm periodicity. (b) (Upper image) Local field enhancement due to plasmonic structure compared with the local field of bare LT-GaAs. Reprinted with permission from [82] Copyright (c) 2015, American Chemical Society.

The work in [82] was further improved by designing an array of plasmonic nanoantenna that works as an anti-reflection coating. Due to a refractive index mismatch between semiconductors and air, light reflection can be up to 30 %. Designing a good anti-reflection coating layer will contribute to a stronger THz signal. Figure 29 shows THz signals from three different plasmonic structures compared with a conventional dipole antenna. All the structures have shown significant improvement, were the plasmonic hexagonal array

achieved the highest current amplitude with 18 times enhancement compared to the conventional dipole and below 10 % reflection [83].

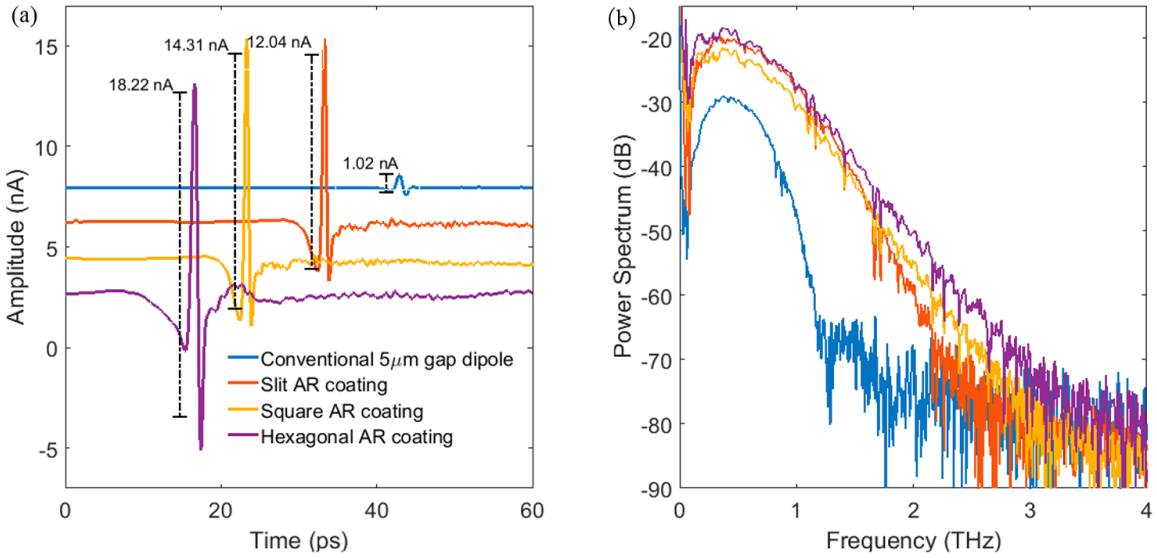

Figure 29: THz time domain signal for the current detected in the receiver. (b) Frequency spectrum of the signals measured in (a). Reprinted with permission from [83] Copyright (c) 2017, American Chemical Society.

Chapter 4 Experimental

4.1 Introduction

In this chapter, the materials and methods used in this work are covered. First, we present the materials that we used in our measurements which include different crude oil samples and two solutions of nanorods. Followed by an explanation for the asphaltene measurement and removal procedure. Finally, the setups and techniques used to measure the LSPR, Raman scattering, and THz-TDS are detailed.

4.2 Materials

For the refractive index and Raman measurement, two bare gold nanorods particles (AuNRs) with different aspect ratios (AR) were purchased from (Nanopartz Inc., Loveland, CO, USA). One has a 3.8 AR and SPR in the range of (765-794) nm (A12-10-780-CTAB), and the second one has 4.5 AR and SPR range of (829-875) nm (A12-10-850-CTAB). In addition, six crude oil samples produced from different oil fields in the world were purchased from (ONTA, Inc. Toronto, Canada) with (24-43) API span. Table 3 summarizes the properties of the samples.

Table 3: Properties of six crude oils from different oil fields used in the refractive index and Raman measurement.

Crude oils	**1**	**2**	**3**	**4**	**5**	**6**
Source	Pennsylvania	Saudi Arabia	Brayan Mound	Iraq	Saudi Arabia	Ecuador
Density	0.81	0.838	0.8454	0.856	0.89	0.91
Sulfur (%)	0.14	1.15	0.33	1.95	2.8	1.31
API	43.2	37.2	35.9	33.7	27.4	24

Different oil samples were used for the THz-TDS measurement as oil with higher asphaltene content is needed. Three crude oil samples produced from different oil fields in the world were purchased from ONTA, Inc. Toronto, Canada with (14.7-29.7) API span and (2.6 - 8.6) % asphaltene content. Table 4 summarizes the properties of these crude oils.

Table 4: Properties of three crude oils used for asphaltene measurement.

	Source	**Density (g/mL)**	**°API**	**Asphaltene (%)**
Oil 1	Ecuador	0.898	25.9	6.82
Oil 2	Venezuela	0.968	14.7	8.63
Oil 3	Iraq	0.877	29.7	2.58

The solvents used in this work are HPLC grade toluene (CAS # 108-88-3) and HPLC grade n-heptane (CAS # 142-82-5), purchased from Sigma Aldrich. Oakville, Canada.

4.3 Asphaltene Measurement and Removal Procedure

The asphaltenes content was measured following the procedure reported in the past [12]. Briefly, 10 grams of the oil were mixed with n-heptane at a volume ratio of (1:40) and left for 2 days in the dark to reach the equilibrium. The mixture was filtered using 0.22 μm membrane filter paper in few consecutive times. The filter cake was washed with hot n-heptane until the effluent was almost colorless. To get the maltene (Oil w/o asphaltene) fluid for each oil, the heptane was vacuum evaporated from the mixture until it reached less than its original weight and no notable change in the weight was noticed with continuing the evaporation.

Also, to get an accurate asphaltene content measurement, the adsorbed maltene and the non-asphaltene solids must be removed from the asphaltenes before weighting. The recovered asphaltenes were dissolved in toluene and the mixture was filtered to remove the non-asphaltene solids. After that, the size of the toluene/asphaltene mixture was reduced by vacuum evaporation. We mixed the reduced size toluene/asphaltene mixture with n-heptane again at a ratio of (1:40) and filtered the solution similarly to the steps above. The recovered asphaltenes dried under vacuum until no notable change in their weight was observed. This method is time-consuming and requires up to 1 L of solvents for a single oil sample. The measured percentage of asphaltene in oil 1, oil 2, and oil 3 are listed in Table 4. Figure 30 shows a picture of the recovered asphaltene on the filter paper inside the funnel, and the asphaltene as a powder after it has been dried.

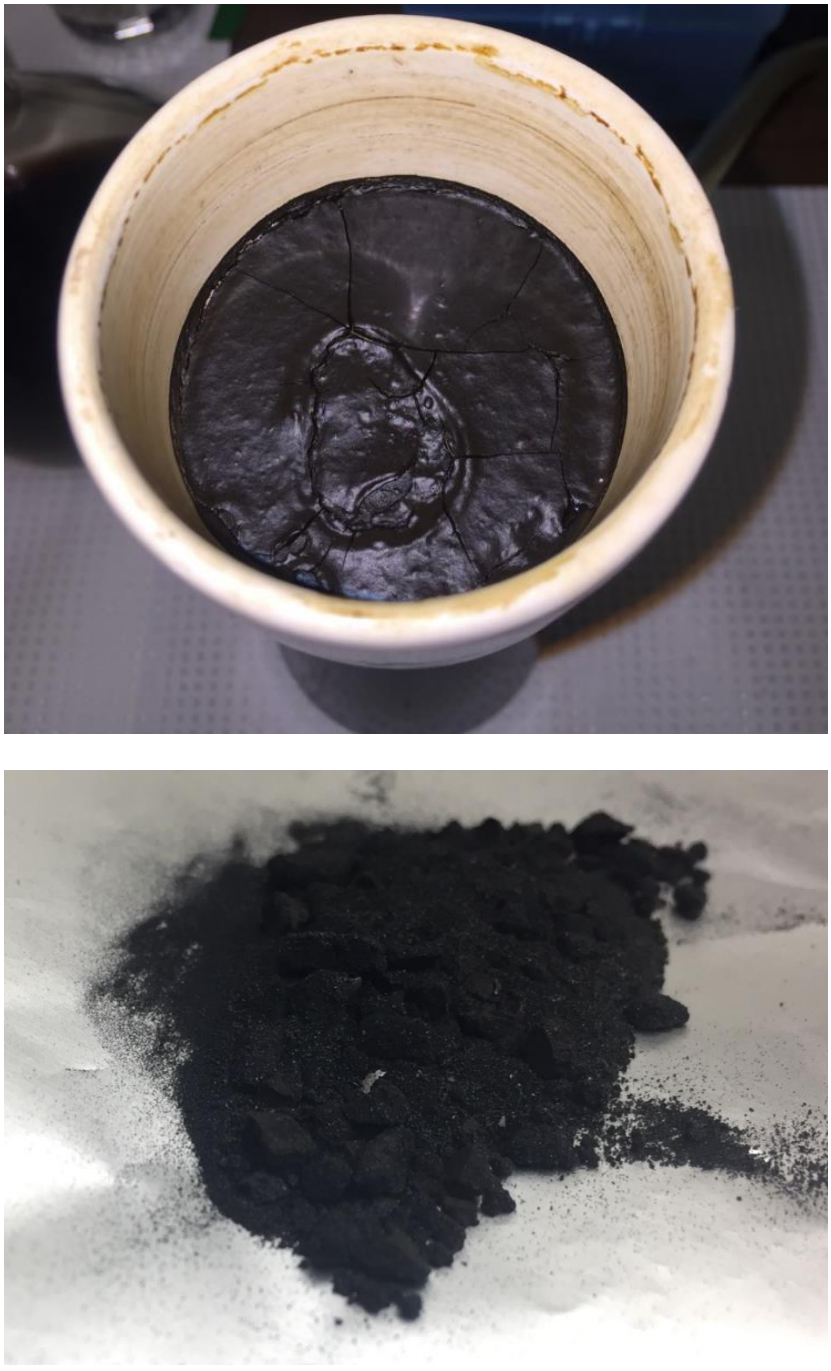

Figure 30: Upper picture shows the filtered asphaltene while still on the filter paper. Lower picture shows the recovered asphaltene on a weighting paper after drying

4.4 Dark Field Experimental Setup

Figure 31 shows a schematic diagram of the optical setup for the Dark-Field (DF) measurements that was previously proposed by our group [84]. White light (LS-1-LL, Ocean Optics Inc.) is collimated via a collimator and a lens then focused onto the sample by a 20 × microscope objective (0.42 NA, Mitutoyo Plan Apo). The objective is placed at 65° from the surface normal. The scattered light from the AuNRs is collected by a 40 × microscope objective (0.68 NA, Zeiss) placed at 10° from the surface normal. The position and angle of these two objectives were chosen to have a minimum light scattering from the air/glass interface to the collection objective. This ensures the measured spectrum is resulting from the light scattered from only the AuNRs themselves. Part of the scattered light from the AuNRs is picked up by the collection objective and is collimated through two lenses in series then focused into an optical fiber tip by another 40 × microscope objectives (0.68 NA, Zeiss). The optical fiber transfers the light to the spectrometer (QE65000, Ocean Optics Inc.) to measure the DF scattering spectrum. Figure 32 shows a picture of the actual setup in our lab.

The AuNRs were immobilized on 80 - 130 μm thick number 0 cover glass (GoldSeal, Ted Pella, Inc) using a drop coating technique. The mechanism of this immobilization is attributed to the electrostatic interaction between the AuNRs particles and the glass. The AuNRs are capped with positively charged CTAB, thus, the repulsive electrostatic force prevents these particles from aggregating, whereas the glass becomes negatively charged

when in contact with a neutral aqueous solution. Therefore, the negative charges on the glass surface attracts the positively charged AuNRs, forming a monolayer of AuNRs on the glass surface [85]. After the drop has dried, the cover glass with the immobilized AuNRs is exposed to plasma oxygen for 5 minutes to remove the CTAB from the AuNRs surrounding. This method has been proven to increase the RI sensitivity up to 37 % in AuNRs [66].

As shown in the inset of Figure 31, a piece of double-sided tape with a circular hole in the middle is placed on the cover glass and the fluid to be measured is put inside the hole, on top of the AuNRs layer. The sample is covered with another cover glass at the top side. This assembled sample is put on a 3-axis stage in a horizontal position where the light comes from the backside, passing through the thin glass to reach the AuNRs. This way the light does not travel through the crude oil and hence the absorption of this high optical density fluid is eliminated. The peak of the spectrum depends on and correlates with the refractive index of the material surrounding the AuNRs at the top of the cover glass, where every increase of the refractive index results in a red-shift of the spectrum. The recorded spectra are normalized to the white light source intensity, filtered using Savitzky-Golay filter in MATLAB to remove the high-frequency noise, and have smoother spectra. Then the peak position is determined using a peak position detection algorithm in OriginLab software.

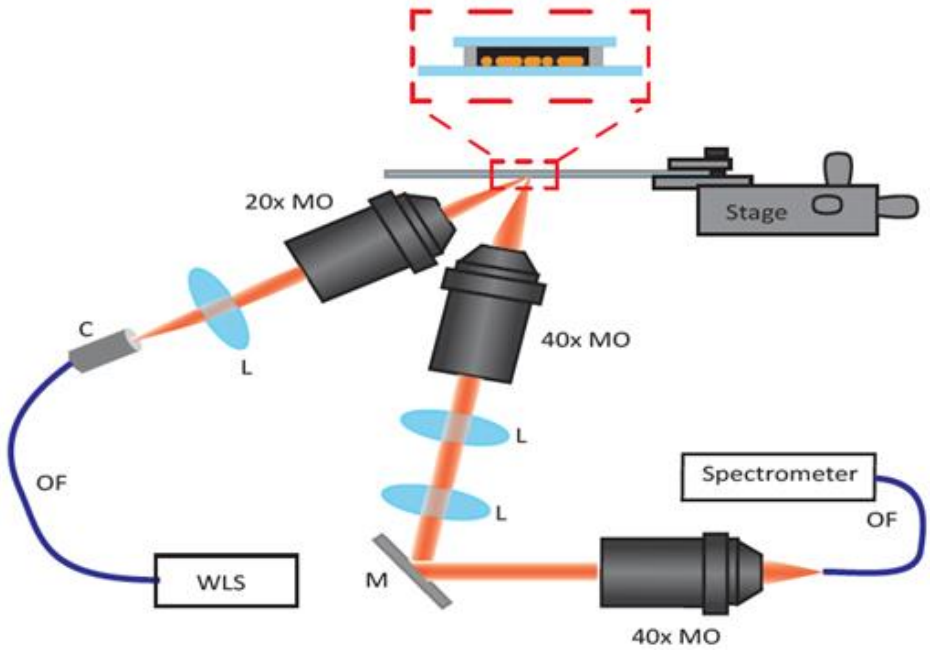

Figure 31: Schematic diagram of the DF measurement setup. WLS is the white light source, L is a lens, OF is an optical fiber, and MO is microscope objective. The inset shows an immobilized AuNRs on a glass slide, and covered with crude oil.

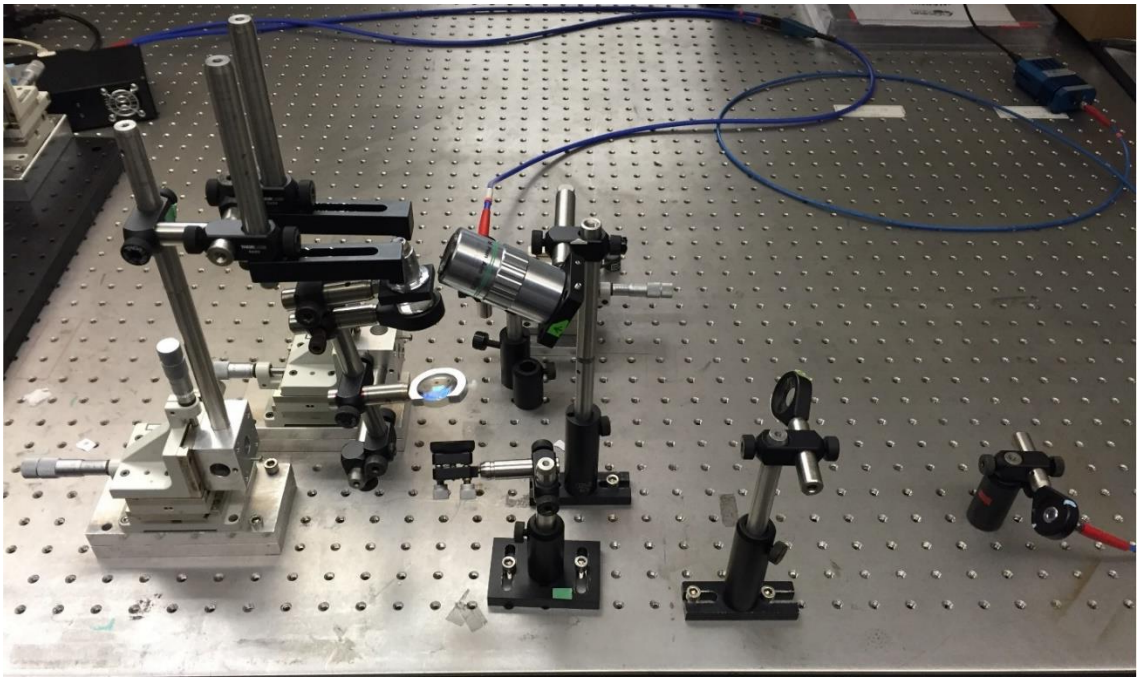

Figure 32: Picture of the DF measurement setup.

4.5 Raman Measurement Setup

Figure 33 shows a schematic of the Raman measurement setup. A portable Raman probe (InPhotonics) was used for excitation and collection whilst the excitation fiber was connected to 785 nm fiber-coupled laser diode (Innovative Photonic Solution) and the collection fiber was connected to a spectrometer (QE65 pro, Ocean Optics Inc.) for detection. The Raman probe was fixed and the sample was mounted on a 3-axis stage to allow the spectra measurement at different locations. The power of the laser was about 3 mW and the integration time was 3s with averaging of five scans in each spectrum for all the samples. The low wavenumber cannot be measured with this probe because of the wide bandwidth of the Rayleigh filter. Therefore, we have used a different apparatus (Renishaw Raman System) that has capabilities to measure Raman spectrum down to 10 wavenumbers. This machine was used to investigate if asphaltene has low-frequency vibrations modes, that often exist in molecules in its size.

The SERS substrate used in this measurement was similar to the one used for LSPR measurement, which was explained in the previous section. However, the drop-coating process was done multiple times in this case. The reason was to increase the density of the AuNRs on the glass to increase the chance for the Raman signal coming from molecules present in the vicinity of the particles where high SERS enhancement is expected. Also, to increase the chances of plasmonic coupling between AuNRs and further increase the SERS enhancement.

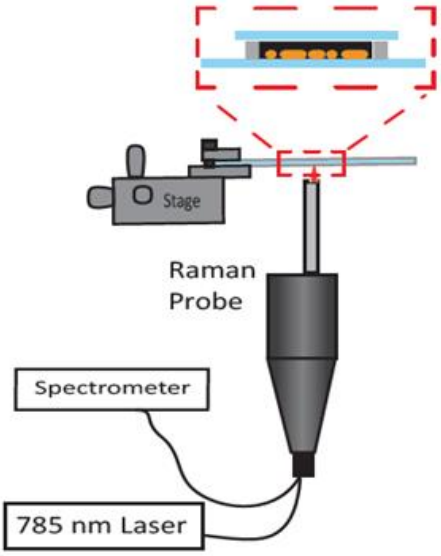

Figure 33: Schematic diagram of Raman measurement setup

4.6 THz-TDS Measurement

Figure 34 shows the (THz-TDS) measurement setup used in this work. The measurement was done in transmission configuration for free space spectroscopy [17-19]. A 780 nm 80 femtosecond laser (Calmar) was used as a pump and probe beams to generate and detect a THz signal. To get a higher THz bandwidth, we have used a Photoconductive Antenna (PCA) previously reported [83] as a transmitter and a commercial PCA purchased from (BATOP, PCA-40-05-10-800-a) as a receiver. The length of the probe beam path varied with a delay-line to change the spectral position of the (THz-TDS) waveform. To achieve a higher resolution frequency spectrum, the scanning length was set to 30 mm, which corresponds to~200 ps. The transmitter PCA was biased with 80V and the pump beam was chopped at 10 kHz. The signal from the receiver PCA was sent to a lock-in amplifier and then to the computer for processing. We used a sample holder made of Teflon (PTFE) as

this material has little absorption in the THz range [86]. The holder width is 10 mm and it can hold a sample of approximately 2.5 mL. The whole setup was enclosed in a glass box and purged with Nitrogen until the relative humidity was less than 3 %.

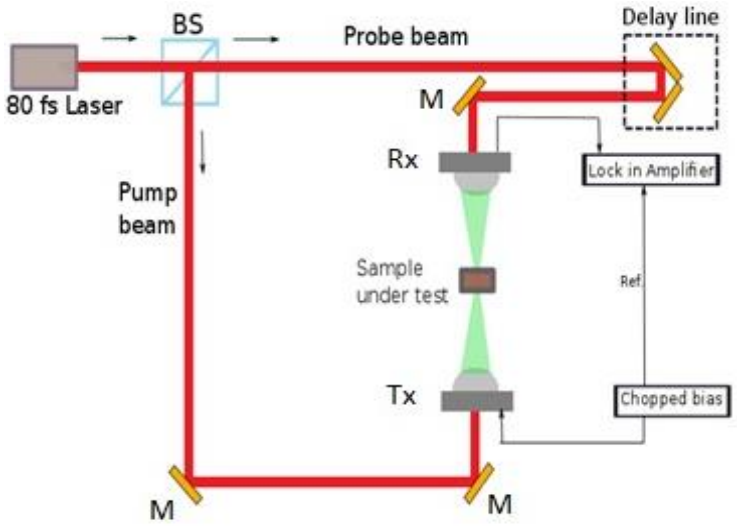

Figure 34: Experimental setup for THz-TDS. BS—beam splitter; M—gold mirror; Tx—transmitter; Rx—receiver.

4.6.1 THz-TDS Setup and Alignment

Choosing from different setup configurations that can be used for THz-TDS, we used a simple line of sight configuration. This configuration is favorable for spectroscopy, but its alignment and signal optimization can be challenging. The dipole in the transmitter and receiver PCAs, which has a dimension of few tens of micrometers, must be exactly in line of sight and parallel to each other for producing the best THz signal. Therefore, building and aligning the setup has to be done carefully. The following six points summarize the main steps in making and aligning THz setup. The steps are illustrated schematically in Figure 35.

1. The first step is to ensure the laser beam is perfectly horizontal and parallel to the optical table. This can be checked by using an optical iris with a small aperture and comparing the height close to the laser output and the end of the optical table. If there is a deviation, a mirror should be inserted in the setup to re-align the beam.

2. A beam splitter (BS) is needed for splitting up the light into a pump beam and a probe beam. It is important to align the BS carefully so that these two beams are exactly perpendicular to each other and are parallel to the optical table.

3. In this step, a retroreflector is installed on a motorized delay line. The retroreflector is a device that reflects light exactly parallel to the incident light, therefore, this device itself is not sensitive to the alignment. However, the motion direction of the delay line must be perfectly parallel with the laser beam. If there is a small angle, the reflected light is still parallel to the incident but there will be a slight change in distance between these two beams. The width of the dipole is usually 5 μm and this slight change can take the laser spot out of the active area. This can be checked by using a laser viewing card at a slight angle w.r.t light direction a few meters away from the delay line. The laser spot shown on the card should be monitored when the delay line is moving from one end to the other. If the spot location is changing, the delay line needs further alignment until the spot is completely stable at one position.

4. The next step is aligning the pump and probe beams. This is done by inserting mirror 1 to redirect the probe beam coming from the delay line and inserting mirror 2 and 3

to redirect the pump beam coming from the BS. As shown in Figure 35 (4), the two beams reflected from mirrors 1 and 3 must be traveling in opposite directions in the same height with no divergence, and meet exactly at the same point. This is important to ensure the PCA antennas will be in the line of sight to each other when inserted.

5. Once the pump and probe beams are aligned, two optical lenses are inserted to focus the light on the dipole of the transmitter and receiver PCAs. Lenses with a large numerical aperture are preferred as they give a smaller laser spot size, enabling us to focus more light on the dipole gap of the PCA. After that, the PCAs are inserted and adjusted with the 3-axis stage to bring the PCA dipole to the optical lens focal point. This can be checked by biasing the PCA and measuring the induced photocurrent. When the laser focal point hits the dipole gap, it will generate the highest photocurrent.

6. At this point, the setup should be initially aligned. For the receiver PCA to detect the THz radiation, the probe pulse and THz pulse must arrive at the dipole gap at the same time. As it can be seen in Figure 35 (6), the movement of the delay line will adjust the paths B1 and B2. Therefore, the delay line can be adjusted so that these two paths are equal by the condition (A1+A2+A3+A4=B1+B2+B3+B4) and subsequently initial THz signal can be detected by measuring the receiver PCA photocurrent. After detecting the first signal, the two PCAs can be adjusted to optimize the signal.

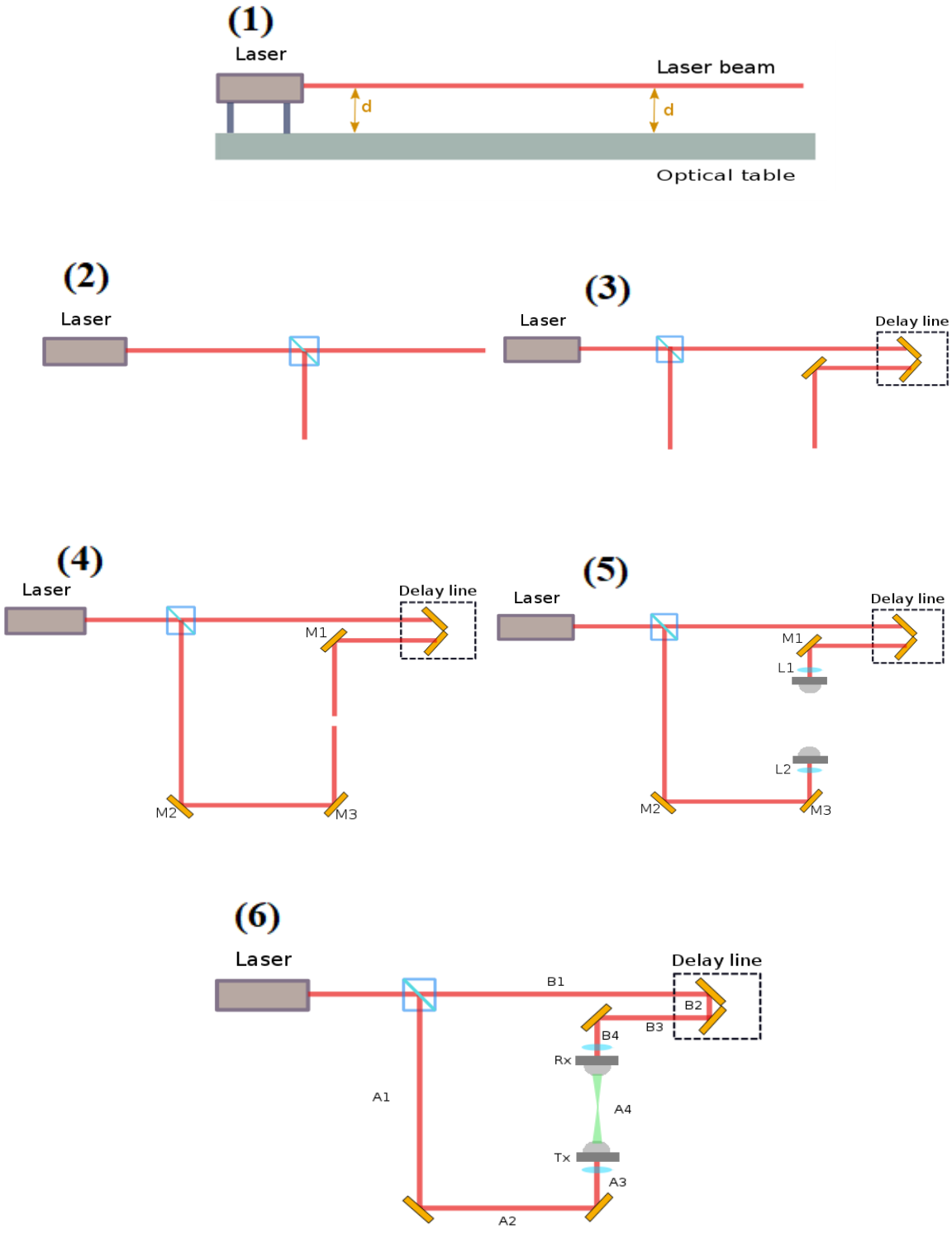

Figure 35: Schematic illustration of the main steps building THz experimental setup. The pictures illustrate the alignment of (1) the laser beam height, (2) Beam splitter, (3) delay line, (4) pump and probe beams, (5) optical lenses and PCAs, and (6) measurement and optimization. (1) is a side view and (2-6) are top views.

4.6.1 Data Acquisition and Analysis

The measurement of the THz signal is done by measuring the photocurrent in the receiver PCA. This PCA is connected to a lock-in amplifier and its output is connected to a data acquisition card (NI-USB 6211) which works as an interface between the computer and the lock-in amplifier. A software from (TeTechs, Inc. Waterloo, Canada) is used for data acquisition and controlling the start position, end position, and the speed of the delay line, in addition to the resolution of the signal (Figure 36). The software also translates the displacement of the delay line into a time stamp for the measured current. The delay line in our setup can travel up to 50 mm, which corresponds to~332 ps time. The spectrum of the measured signal is determined by taking the fast Fourier transform over the measured time interval.

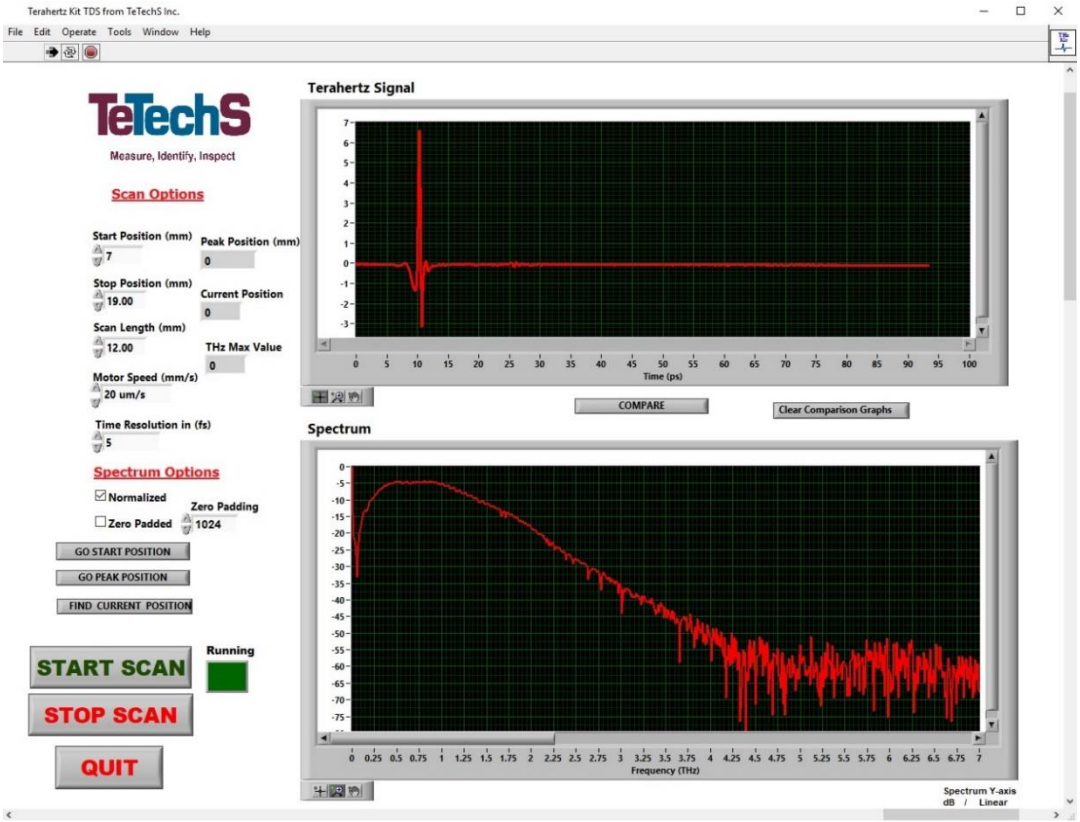

Figure 36: THz data acquisition software Interface

Figure 37 shows the THz time domain waveform of the empty sample holder in an ambient condition and after it has been purged with nitrogen. Figure 37 (b) shows the corresponding frequency domain spectrum where no absorption lines can be observed when the box was purged with nitrogen. Note that there is a slight oscillation that can be observed in the spectrum. This is called etalon effect and caused by the echoes in the time domain signal due to internal reflection in the walls of the sample holder.

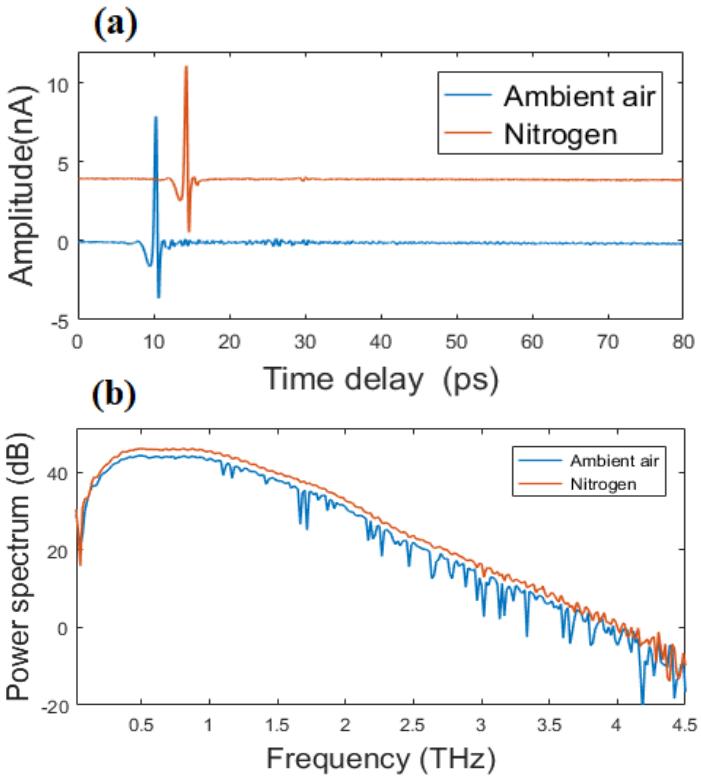

Figure 37: Time domain current signal detected at the receiver in an ambient condition and when the system was purged with Nitrogen. The nitrogen curve is offset for clarity. (c) THz Power spectrum for the result in (b)

The ultimate goal of this work is to measure the materials optical parameters, namely the refractive index and absorption in the THz frequencies. This requires taking a reference

scan of the empty sample holder and measurement scan when the fluid is inside the holder. A MATLAB code was written (Appendix A) to calculate these coefficients using the Eq. 2.18 and 2.20.

Chapter 5 Results and Discussion

5.1 Crude Oil Refractive Index

Here, we have used nanorods to characterize different crude oils from various sources around the world with (24 – 43) API° span. The achieved sensitivity was (247.7 nm/RIU) which corresponds to 0.013 RIU resolution. The refractive index has been determined by measuring LSPR peak in the Dark-Field (DF) spectrum of the nanorods. The nanorods have been immobilized on a glass slide and covered with the fluid to be measured. The measurement took place from the back side of the glass slide. This method uses a simple and flexible optical configuration, and yet it can eliminate the effect of the absorption when measuring very high optical density fluids as the light reflected from the nanorods themselves, not the fluid. Also, the measurement is not sensitive to the variation in the light source intensity as we are interested in determining the peak position only.

5.1.1 Sensitivity of Gold Nanorods to Refractive Index

The first step in this work was to measure the sensitivity of both AuNRs that we have used and establish a calibration equation to calculate the refractive index of an unknown sample. To do so, following the approach reported in the literature [6], we have measured the LSPR of different fluids with known refractive index. The fluids were a mixture of water-glycerol

with different volume ratios varied from 0% to 100% at six steps (16.66% each). The refractive index of the mixture was calculated by the Lorentz-Lorenz equation where the refractive index of water is 1.333, and the refractive index of glycerol is 1.475. Figure 38 shows the relationship and the values between the glycerol concentration in the mixture and the refractive index. In addition to that, immersion oil with refractive index 1.515 was used for higher RI measurement.

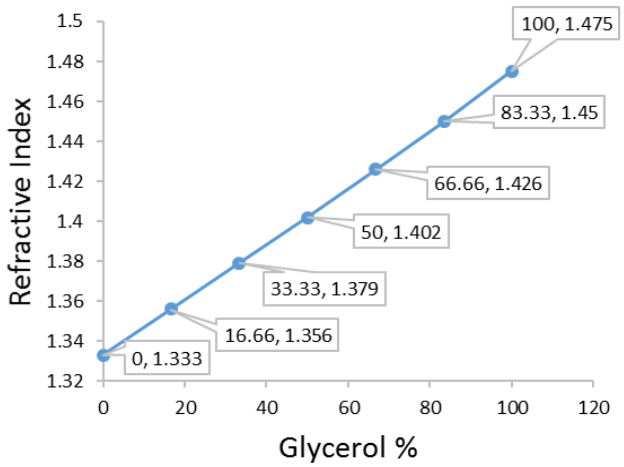

Figure 38: The relation between the Glycerol percentage and the Refractive index

Figure 39 shows the extinction spectra of both AuNRs (3.8 AR and 4.5 AR) in their original aqueous solution. The NR with 3.8 AR has an LSPR peak at 785 nm, and the NR with 4.5 has an LSPR peak at 826 nm. The linear relation between the LSPR peak and the aspect ratio is well established in the literature and can be calculated by $\lambda_{max} = 96AR + 418$ [87]. Based on this relation, we have verified the aspect ratio of both AuNRs and we found that the LSPR peak of the second AuNRs corresponds to 4.3 AR instead of 4.5 AR, which is available from the manufacturer. However, we will continue to refer to them as AuNRs with 4.5 AR for consistency. The dashed light in the Figure represents the laser wavelength,

785 nm, used in the Raman measurement. The laser falls on the resonance of both AuNRs and therefore either one of them will produce SERS enhancement.

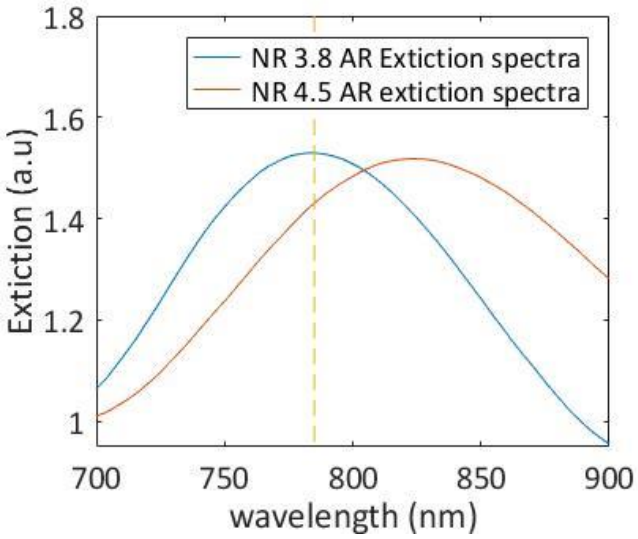

Figure 39: Extinction spectra of 3.8 and 4.5 AR AuNRs. The dashed line represents the laser line used for SERS measurement.

We know from the literature that 3.8 AR AuNRs will have less sensitivity than 4.5 AR AuNRs, [6] however we have measured the sensitivity of both AuNRs to ensure that the setup works well, and the results are consistent. For that reason, we have used fewer points for the 3.8 AR AuNRs. Figure 40 (a) shows the scattered spectra of the DF measurement of the 3.8 AR AuNRs covered with different fluids. As the refractive index of the fluid surrounding the AuNRs increases, the LSPR peak is red-shifted accordingly. When the refractive index of the surrounding media decreases, for example in the case when no fluid is on top the AuNRs (air), the LSPR peak will be significantly blue-shifted. Figure 40 (b) shows the DF measurement for the 4.5 AR AuNRs covered with eight different fluids, water-glycerol mixture with 16.66 % glycerol increase each step and immersion oil. As expected, the red-shift is larger in the 4.5 AR AuNRs than the 3.8 AR AuNRs.

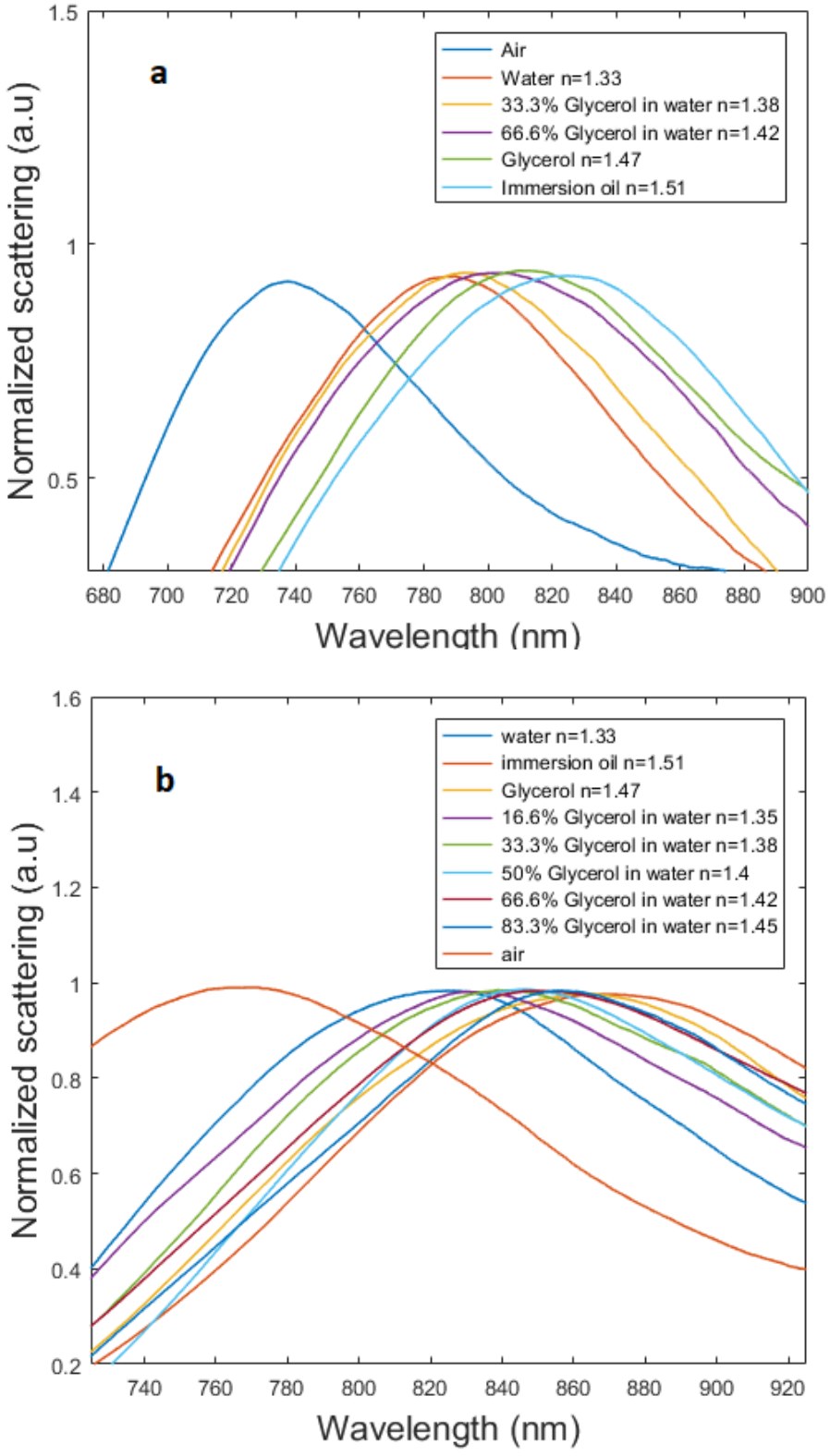

Figure 40: (a) DF spectra of AuNRs 3.8 (aspect ratio) in different fluids. (b) DF spectra of AuNRs 4.3 (aspect ratio) in different fluids.

Figure 41 shows the relation between the refractive index and the LSPR peak changes for the measurement shown in Figure 40 (a & b). The orange line refers to the 3.8 AR AuNRs and the blue line refers to the 4.5 AR AuNRs. From the slopes, the sensitivity of both was determined and they are 205.8 (nm/RIU) for the 3.8 AR and 247 (nm/RIU) for the 4.3 AR. It can be noted that there are some variations in the reported sensitivity of AuNRs in the literature, but these results are comparable to what has been reported, even with the reduction that is expected in the sensitivity from the AuNRs contact with the glass substrate. Wang, C.R.C. group has measured the sensitivity of AuNRs immobilized on a glass substrate, and it was approx. 260 and 366 (nm/RIU) for 4.6 and 5.2 AR respectively [88]. Wang, J. F. group has reported 195, 224, and 288 (nm/RIU) index sensitivity in a solution for 2.4, 3.4, and 4.6 AR AuNRs respectively [6]. The same group in a later report has found that the sensitivity of AuNRs does not only depend on the aspect ratio but depends on the size of the AuNRs too, bigger AuNRs with the same AR achieved higher sensitivity [7]. Erik Martinsson, et al. reported 385 (nm/RIU) for AuNRs with 3.5 AR in solution and this has dropped to 255 (nm/RIU) when immobilized on glass, this reduction in the sensitivity is expected to up to (34%) in AuNRs [66]. Wang, J. F. has attributed the variation in the sensitivity to the differences in the apex of the AuNRs. Sharper apex will result in higher sensitivity, therefore, the reproductivity of the sensitivity can be variable as different synthesis methods may produce slightly different apex [6].

In our experiment, we have chosen the 4.5 AR AuNRs to measure the crude oil refractive index since it has higher sensitivity. The relation between the refractive index and the LSPR peak is derived from the plot in Figure 41 and the equation used is the following.

$$RI = (LSPR_{peak} - 497.52)/247.7 \quad (5.1)$$

In addition to sensitivity, the resolution is a key measure when evaluating any sensor performance. The resolution can be calculated by taking the ratio between the smallest detectable change in the output of a sensor and the sensitivity of the sensor. Therefore, In the ideal case the resolution can be determined by dividing the spectrometer resolution, 0.75 nm in this case, by the sensitivity, 247.7 (nm/RIU) in this case, and the resolution will be 0.003 RIU. However, in reality, there are extra sources of noise and variations that lead to less resolution. More reliable approach is to measure an SPR sensor resolution is to calculate the noise standard deviation (STD) and divides it by the sensitivity [89]. The average STD in our measurement was 1.62 nm which corresponds 0.0065 RIU. But because this approach is based on noise measurement, the resolution is often multiplying by a confidence factor. We considere a confident factor of two and accordingly the resolution is 0.013 RIU. Now despite the widespread reports that used NPs for sensing, researchers often report only the sensitivity of their results, thus, there is a lack data in the literature about the resolution of NPs based sensors to compare our results with.

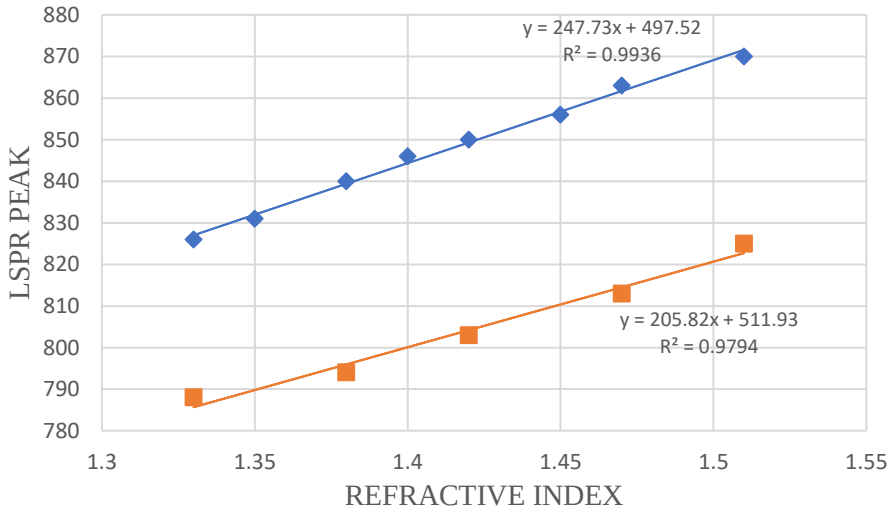

Figure 41: The sensitivity of AuNRs with two different aspect ratios. The blue line is the AuNRs with 4.5 AR, and the orange line is the AuNRs with 3.8 AR.

5.1.2 Crude Oil Refractive Index Measurement

Figure 42 shows the scattered spectra of the DF measurement of the 4.5 AR AuNRs covered with six different crude oil that is listed in Table 3. It can be seen that each oil has a different LSPR peak and hence different refractive index.

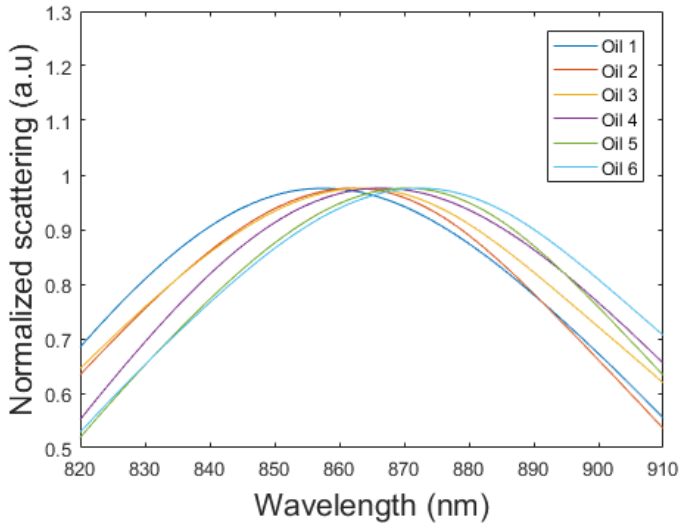

Figure 42: DF spectra of 4.5 AR AuNRs covered with six crude oils

Table 5 shows the LSPR peak position for each oil and the corresponding refractive index calculated by Eq. 5.1. The plot in Figure 43 shows the relation between the crude oil density and the calculated refractive index for each crude oil. The linear relation between the density and the refractive index is clear and in agreement with previous reports [4,48].

Table 5: Crude oil Refractive index calculated by Eq. 5.1

	Density	API	LSPR peak	Refractive Index
Oil 1	0.81	43.2	857.5	1.453
Oil 2	0.838	37.2	862.2	1.472
Oil 3	0.845	35.9	864.1	1.480
Oil 4	0.856	33.7	866.5	1.490
Oil 5	0.89	27.4	870.3	1.505
Oil 6	0.91	24	872.5	1.514

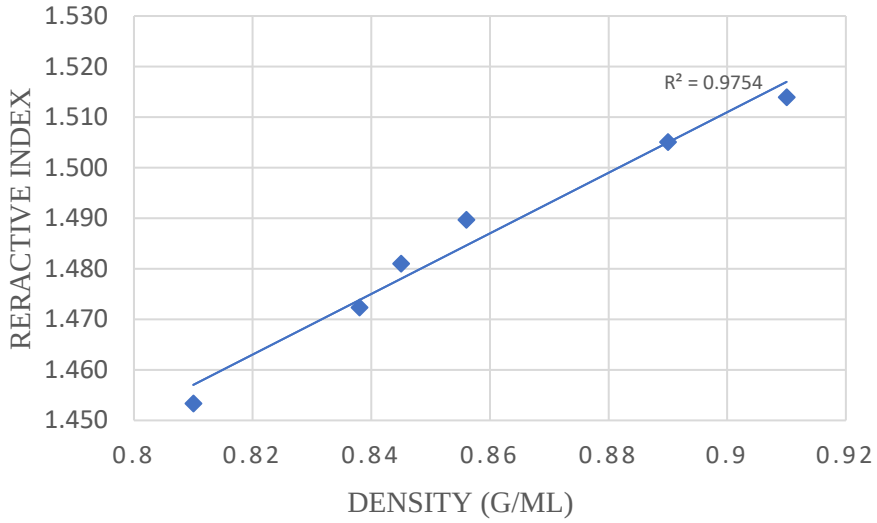

Figure 43: Relation between the Density and the calculated Refractive index of different crude oils.

The refractive index is a property of interest as it can give insight into the quality of the crude oil. Also, many physical and thermodynamic properties can be inferred from the refractive index measurement [3]. The objective of this work was not to achieve the highest sensitivity or resolution of refractive index measurement but to shine the light on the advantage of using nanoparticles to characterize crude oil. Unlike the measurement of biological and biomedical species where super high resolution is in need, the crude oil refractive index measurement needs only modest resolution, but the challenge is to develop a sensor that works well with high refractive index, high optical density fluids. The sensitivity that we have got in this measurement (247nm/RIU) can be increased significantly simply by just increasing the aspect ratio of the nanorods or using different nanoparticles such as nanopyramids. By using more sensitive spectrometer or/and more sensitive nanoparticle, the resolution can be comparable or outperform what has been

achieved using conventional surface plasmon resonance based on Kretschmann configuration [48]. The advantage of this approach is that the scattered spectra are coming from the nanorods that are in contact with the substrate, that means the high absorption nature of the crude oil will not affect the measurement. This will make it possible to measure very heavy oils that was not attainable with standard refractive index refractometers. The configuration of this measurement can be altered for more simplified dark-field measurements where only one objective is used in the normal configuration.

5.2 Crude oil Raman Spectrum

In this section, Raman spectroscopy has been used to study different crude oils shown in Table 3. The first step was to measure pure Raman spectra of these samples without using SERS as shown in Figure 44 (a). There was an intense fluorescence background that we think will overwhelm the majority of the Raman bands. However, there are still some features that can be seen in the (1200—2000) wavenumber range. Therefore, the nanorods have been used to measure SERS spectra.

Figure 44 (b) shows the SERS spectra of these six crude oils. The peaks in SERS spectra are much stronger than the pure Raman signal but there is a great deal of similarity between the enhanced Raman signals, which make it not suitable to distinguish one crude oil among others. The fluorescence background has always been extremely problematic to Raman measurement [27]. Even though we have used a NIR laser (785 nm), the oils have produced a significant amount of fluorescence which has often saturated the spectrometer. To reduce the fluorescence effect and have a better SERS spectra, we found it useful to use low power

(~ 2—3 mW) to produce better SERS spectra Also, as discssed in section 4.5, we have increased the density of the AuNRs on the substrate. That is important to ensure that more Raman signals are coming from molecules in the vicinity of the AuNRs or between two adjusted particles where they experiences large Raman enhancement and at the same time less fluorescence signal are coming from the bulk fluid.

For better understanding of this measurement, we have subtracted the background fluorescence from the spectra and as a result of that, the peaks were clearer (Figure 44 (c)). We have tried to analyze these spectra and find a relation between the peaks intensity, ratios, or size and correlate them with other oil properties, but no useful information was found. Principal component analysis (PCA) is a unique technique that often used to characterize data with high similarity and has been used with Raman spectroscopy widely [90]. Using PCA did not reveal extra information and we think at this point that Raman spectra are not suitable to differentiate different oils.

However, one positive aspect of this is that this range of Raman shift can be used as a clear fingerprint in detecting hydrocarbons. In some application, it is crucial to confirm the presence of hydrocarbons during the exploration stage. SERS fingerprint can fulfill this purpose or at least can be a good complementary tool to the existing methods, such as fluorescence, and IR in detecting and confirming the presence of crude oil.

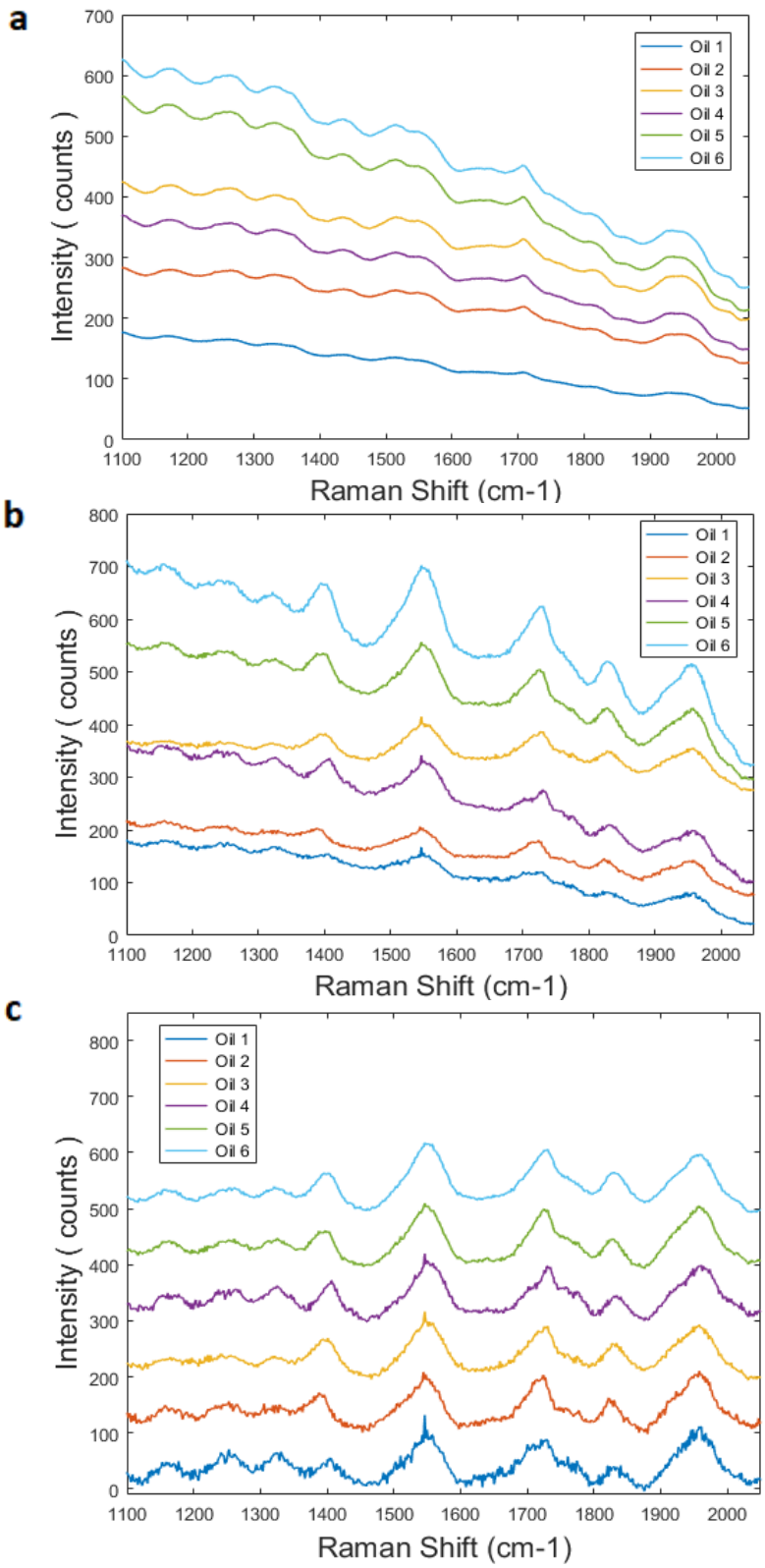

Figure 44: Spectra of six crude oils in Table 2 (a) Bare Raman spectra, (b) SERS enhanced Raman spectra, (c) SERS enhanced Raman spectra after fluorescence subtraction

In a subsequent step, we have measured two different crude oils with and without asphaltene using the Renishaw Raman System. This system is capable of measuring low wavenumbers Raman, which often give useful information about the molecular structure of the material. Figure 45 shows the Raman spectra in (10-200) wavenumber range for two samples. Unfortunately, the intense fluorescence is covering any potential Raman feature, making Raman low wavenumber data option not useful when studying crude oil.

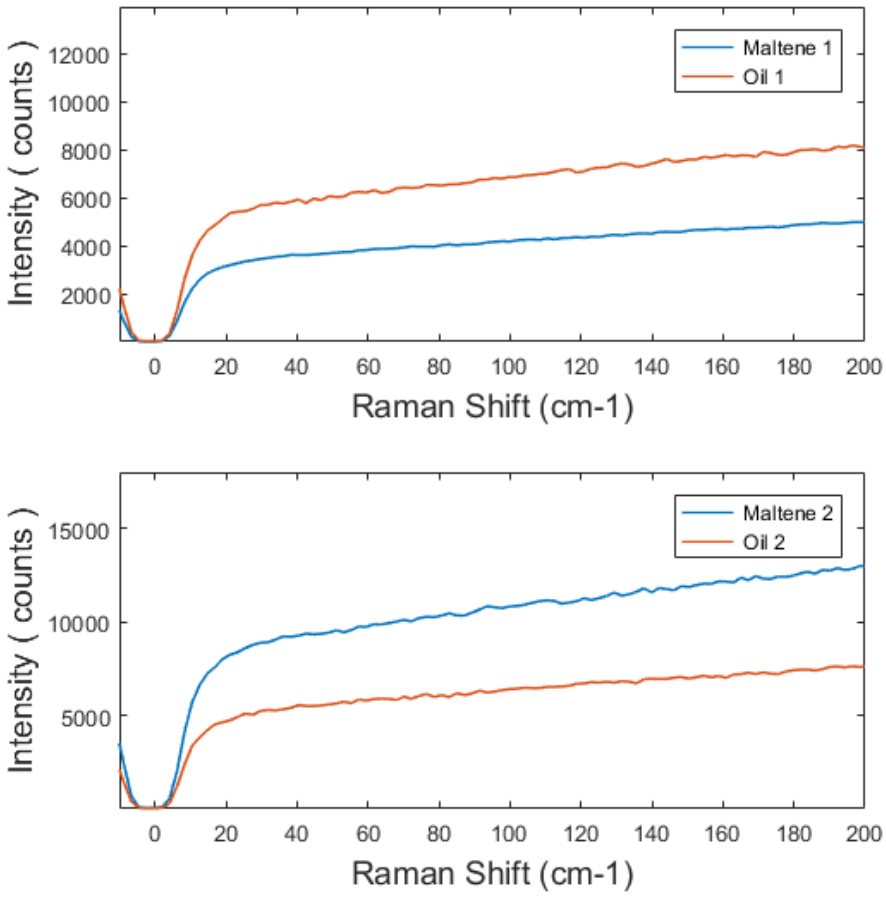

Figure 45: Low wavenumber spectra for two different oil with and without asphaltenes

5.3 Asphaltene Characterized by Terahertz

In this part of my work, we have studied asphaltenes using THz-TDS with more attention for relatively high asphaltene content crude oils. Our approach was to investigate the effect of the asphaltene fraction on the THz signals of the crude oil. To do that, we have compared both the THz time domain signal and frequency domain spectrum between the neat crude oil and the de-asphaltened crude oil samples (maltene) of three different oils (Table 4). We found that the difference in the time delay of the peak of the THz time-domain signal correlates well with the asphaltene content of the crude oil. On the other hand, the absorption of the time domain peak signal seems to correlate as well with the asphaltene content but with less sensitivity. We have also noticed that the crude oil frequency domain spectrum has absorption lines that match the lines of the water. These absorption lines disappear when the asphaltenes have been removed from the oil.

5.3.1 Crude Oil and Maltene THz Time-Domain Spectra

Figure 46 shows the time domain waveform of the reference scan (empty sample holder), neat oil, and the deasphaltened oil (maltene) of oil 1, oil 2, and oil 3 respectively. There are few observations that can be seen in both the peak time and the peak amplitude. First, we can see that there is a negative shift in the time delay for all the oils between the neat oil peak time and the maltene peak time. This shift has a linear relation with the asphaltene concentration of each oil as shown in Figure 47. The result indicates that this method has the potential to be used to measure the asphaltene content in a similar procedure to what has been reported before using optical spectroscopy [9]. In that way, the measurement can

be done within approximately 2-3 hours and consume significantly less solvent and oil samples with accuracy that could outperform the traditional gravimetric methods.

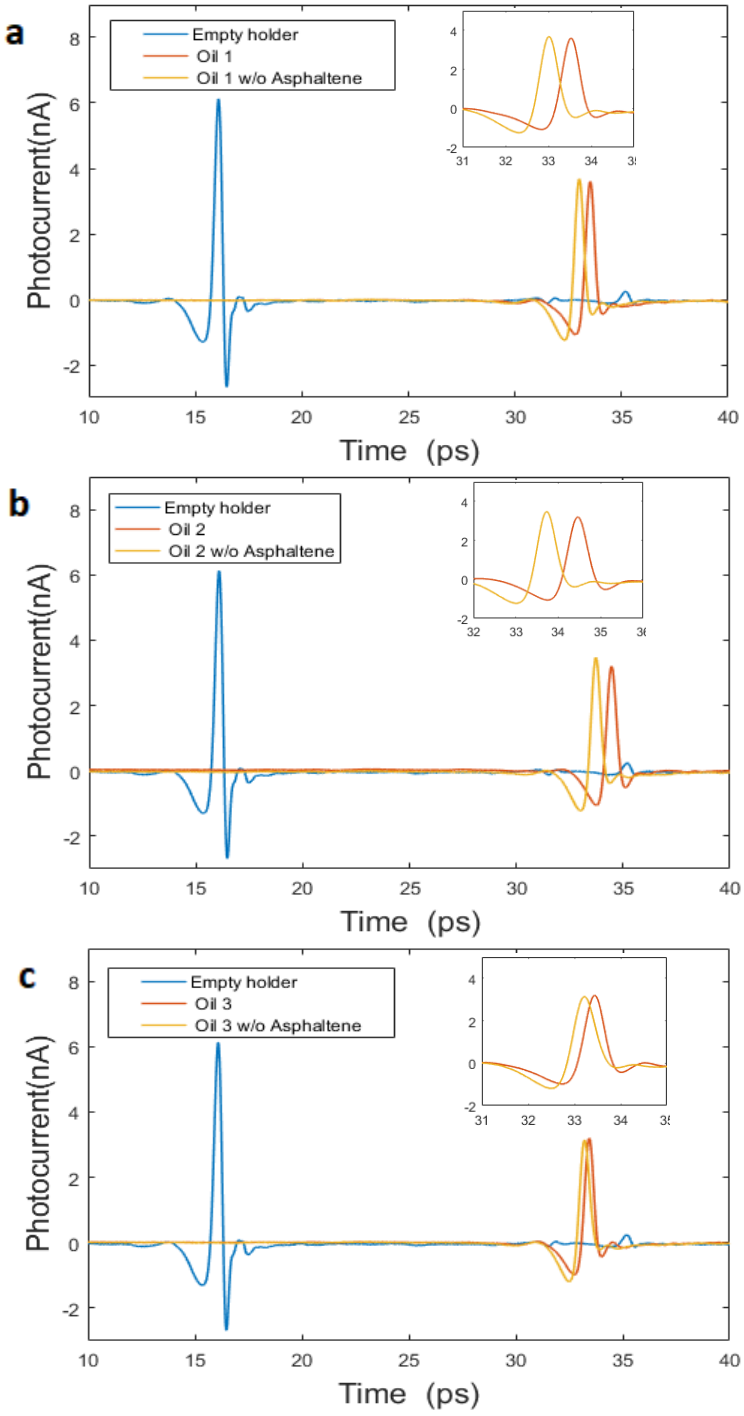

Figure 46: THz time domain signals for reference, oil, and maltene of (a) oil 1, (b) oil 2, and (c) oil 3.

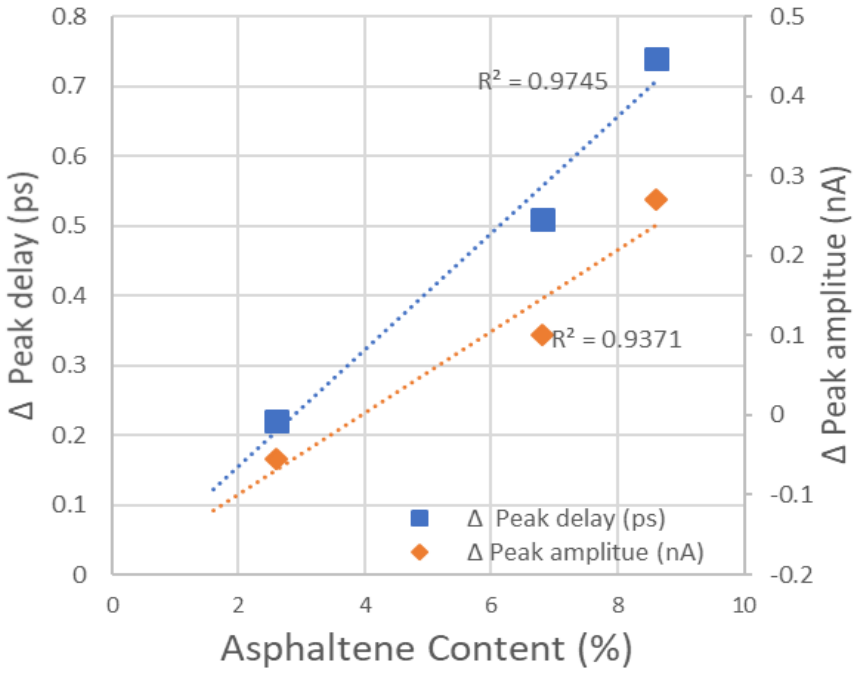

Figure 47: Relation between asphaltene content and peak time delay and absorption change.

Based on the sensitivity of this result which is 0.083 ps per 1% asphaltene content and the standard deviation of the measurement which is 0.012 ps, the asphaltene limit of detection (LOD) calculated to be 0.43% by taking the LOD to be 3 times the standard deviation. Because the crude oil absorption in the THz frequencies is very moderate, this LOD can be easily boosted by just increasing the oil sample thickness. For example, by increasing sample thickness from 1 cm to 5 cm, which will still result in a detectable signal, the LOD will go down to 0.08%.

The second observation here was the change in the peak amplitude between the neat oil and the maltene. The positive peak amplitude of oil 1 and oil 2 has increased after removing the asphaltenes from the oil in a linear trend with the asphaltene content. However, this was not observed exactly in oil 3 where the positive peak amplitude decreased slightly after

removing the asphaltenes, but the negative peak has increased by a larger percentage which made the overall peak to peak signal increased. Figure 47 shows the change in the positive peak amplitude as a function of the asphaltene content. The sensitivity of the peak amplitude to the asphaltene content and the standard deviations is 0.051 nA per 1% asphaltene content and 0.032 nA respectively, which corresponds to 1.88% limit of detection. That is more than 4 times worse than the LOD based on the time delay. Because the asphaltenes are the most polar part in the crude oil with dipole moment larger than even the water [92], the change in the absorption due to the asphaltene removal was less than what we anticipated, especially with these asphaltene-rich oil samples. It is also worth mentioning that we are not considering the complex Fresnel transmission coefficients at the sample holder oil interface and the oil sample holder interface. The change in the refractive index due to the asphaltenes removal will change this coefficient slightly and consequently will add some uncertainty to the result.

5.3.2 Asphaltene THz Refractive Index Spectra

The refractive index of the oil and maltene has been calculated directly from the measured time domain signal and subsequently the asphaltene refractive index has been estimated based on these two spectra. The refractive index is calculated by $1 + [\varphi c/\omega d]$ where φ is the fast Fourier transform (FFT) phase difference between the sample and the empty sample holder signals, ω is the angular frequency, c is the light speed in vacuum, and d is the sample thickness [19]. The asphaltene refractive index can be extracted from the data of both the oil and the maltene refractive index spectrum by using the Lorentz-

Lorenz mixing rules [5]. According to this theory, the oil can be considered as a mixture of two component, maltene and asphaltene, and its refractive index is:

$$\frac{(n_{oil}^2 - 1)}{(n_{oil}^2 + 2)} = \frac{(n_{asp}^2 - 1)}{(n_{asp}^2 + 2)}\phi_{asp} + \frac{(n_{mal}^2 - 1)}{(n_{mal}^2 + 2)}\phi_{mal}$$

Where n_{oil}, n_{mal}, and n_{asp} are the refractive index spectra of the neat oil, maltene, and asphaltene respectively. ϕ_{asp} is the asphaltene volume fraction of the crude oil which can be calculated by knowing the asphaltene density [43], ϕ_{mal} is the maltene volume fraction of the crude oil ($\phi_{mal} = 1 - \phi_{asp}$). The n_{asp} can be extracted from this equation since all the other variables can be either measured or calculated.

Figure 48 (a-c) shows the refractive index spectra in the range of (0.3-2.2) THz of the neat oil, maltene, and the asphaltene for oil 1, oil 2, and oil 3 respectively. In general, the spectra show that the refractive index of all the oils have been decreased by a range of (0.02-0.04) after removing the asphaltene. The refractive index of the maltene of oil 1 and oil 3 decreases considerably in the low frequency compared to the neat oil which we attribute to higher asphaltene refractive index in that range. Oil 2 did not exhibit the same feature but instead, the refractive index difference between the neat oil and maltene was almost uniform throughout the spectra. The calculated asphaltene refractive index of the three oils have been plotted together in Figure 48 (d) for comparison. The asphaltene from oil 1 and oil 3 have exponential decay-like spectra and the asphaltene from oil 2 has an almost flat refractive index in the reported range. All the asphaltene refractive index spectra seem to stabilize within the values of (1.75-1.85) in the spectral range of (1.5-2.2) THz. This result indicates that asphaltene from various sources may exhibit different THz spectra, especially in the low THz frequencies.

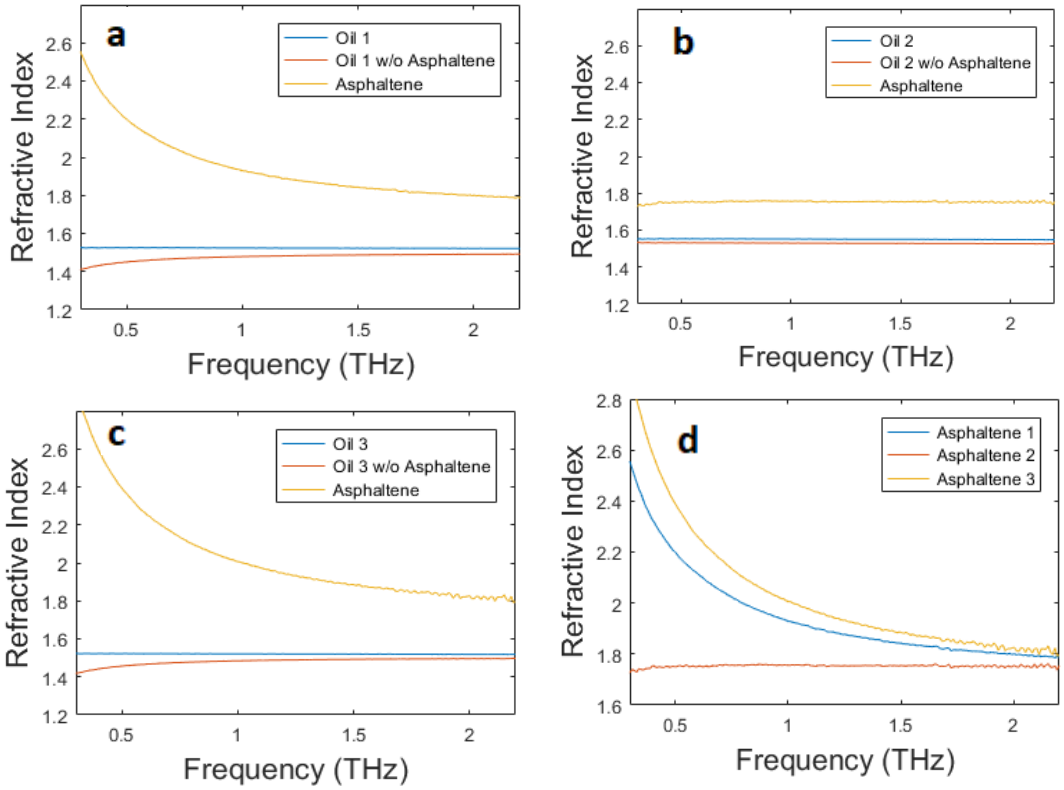

Figure 48: Refractive index of oil, maltene, and asphaltene from (a) oil 1. (b) oil 2. (c) oil 3. (d) comparison of the asphaltene refractive index from the 3 oils.

5.3.3 Crude Oil and Maltene THz Frequency Domain Spectra

After applying the FFT to the time domain signals, the THz frequency spectra of the reference, neat oil, and the maltene were calculated and plotted in the Figures 49 (a-c) for all the oils. The absorption coefficient α has been calculated by $-(2/d)\ln\{T(n+1)^2/4n\}$ where T is the FFT magnitude ratio between sample and reference signals, d is the sample thickness, and n is the refractive index [19]. The Figure 49 (d—f) shows the calculated absorption coefficient of the neat oil and the maltene for the three oils. It can be observed that the absorption of both the neat oil and the maltene of all the oils is increasing almost linearly versus the frequency. The reference signal has a

bandwidth of~4 THz, but because the oil has stronger absorption in the high frequency component the effective spectra has been reduced to less than 2.5 THz as the signal approaches the noise floor beyond this frequency.

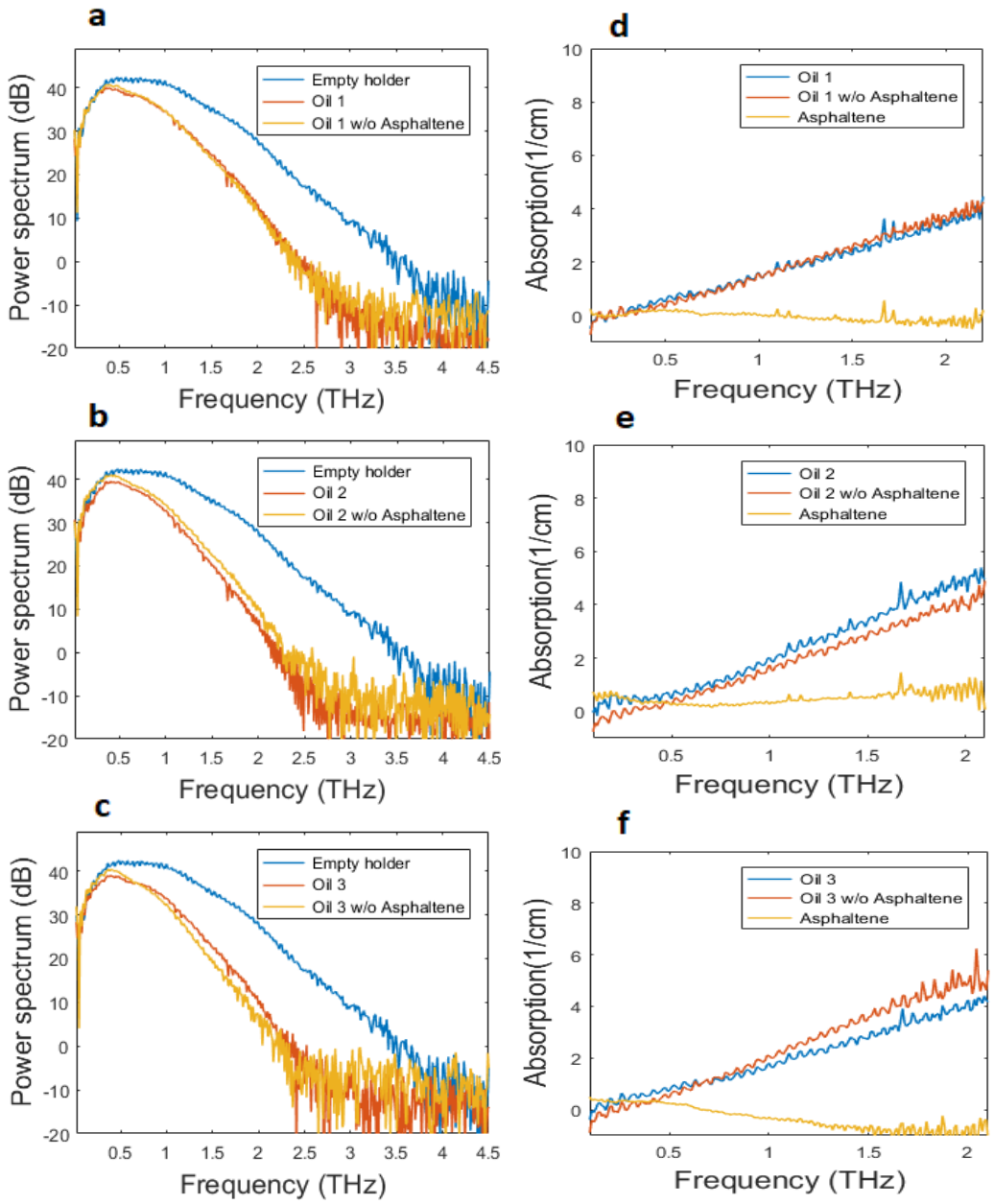

Figure 49: THz frequency domain spectrum for the reference, oil, and maltene of (a) oil 1. (b) oil 2. (c) oil 3. (d), (e), and (f) are the absorption coefficient of oil, maltene, and asphaltene of oil1, oil 2 and oil 3.

5.3.4 Asphaltene THz Absorption Spectra

The Figure 49 (d—f) also shows the difference in the absorption between the neat oil and the maltene, which we attribute to the asphaltene absorption. The asphaltene absorption of the three oils has been plotted together in Figure 50 (a) for comparison. The magnitude of the asphaltenes absorption shown in Figure 50 (a) was moderate even though these crude oil samples contain relatively high asphaltene content. There is still some a linear relationship between the magnitude of the broad absorption and the asphaltene content, like what has been shown in the time domain signal in Figure 47.

In addition, the Figures 49 (d—f) show that there are some narrow absorption lines that were observed in the oil and were absent in the maltene, thus, it can be seen clearly in the asphaltene absorption spectra in Figure 50 (a). Those lines match the water absorption lines to a high degree [92]. The vertical lines in Figure 50 (a) represent the typical water absorption lines, overlap with all the absorption lines of the asphaltene spectra, however, not all the expected water lines are seen in the spectra. The water absorption lines do not appear when probing water molecules as bulk water but instead they appear when measuring water in the vapor phase or when adsorbed on a material at very low quantity to the level that it does not form bulky water [92]. There have been many reports in the literature that confirm the interactions between the asphaltenes and water, though these interactions mechanism is not well understood [56-85]. What is known are that the asphaltene absorbs moisture [93], and the asphaltene content has a linear relation with the water content of the crude oil [94].

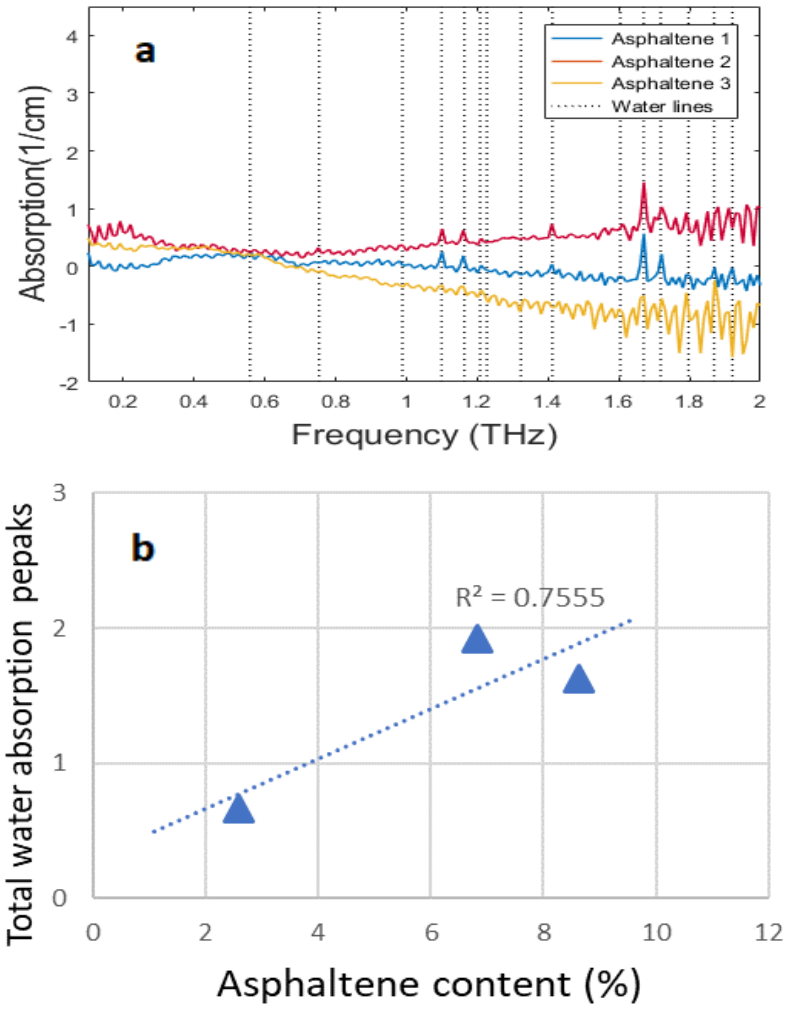

Figure 50: (a) Comparison of the asphaltene absorption from 3 oils. (b) The total intensity of the water lines measured in (a) versus the asphaltene content.

Based on measurement data and the literature background, it may be inferred that these lines are from scattered water molecules in the oil that was adsorbed on the asphaltenes and that the water was removed during the asphaltene separation process. In addition, the fact that there is a reasonably linear trend, as shown in Figure 50 (b), between the absorption of the water lines and the asphaltene content make us lean more toward this conclusion.

The high optical density of crude oils and asphaltenes made it challenging to measure their refractive index and absorption in the visible and NIR range without excessive dilution [5,9]. On the other hand, the mild absorption of the crude oil and asphaltene in the THz frequencies made it possible to measure thick samples in the transmission configuration. The result of this work shows the potential of the THz-TDS to be used in the future in various application such as measuring asphaltene content, asphaltene precipitation onset, and asphaltene yield curve.

Chapter 6 Summary and Future Work

6.1 Summary

In this work, we have investigated few optical spectroscopies to study crude oils and its asphaltene.

We have used nanorods to measure the refractive index and to enhance the Raman spectrum of different crude oil samples. Nanorods can be used to measure the refractive index of these high optical density fluids. This method is simple, and the high absorption of the heavy oil will not affect the measurement. The Raman spectrum was sufficiently enhanced by using nanorods, the bands did not show any qualitative or quantitative information to differentiate different oil samples.

In the second part, THz-TDS was used to study asphaltenes in different crude oils. The difference in the time delay and the peak amplitude between the neat crude oil and the maltene correlated linearly with the asphaltene content. Variation was found in refractive index spectra of the asphaltene from different oils in the low THz frequencies and comparable spectra in the higher frequencies. The absorption coefficient spectra show a mild absorption due to asphaltene with no clear feature except some narrow absorption lines that we attributed to water molecules adsorbed on the asphaltene. The water molecules provide a more specific (albeit proxy) spectral feature for asphaltene in oil but do not show as good linearity as refractive index and absorption variations.

6.2 Future Work

This work was to shine the light on different methods to characterize the oil, but there are still much more that can be done to improve the current results or to extend it to a new application.

For nanorods

- Even though the resolution of the refractive index measurement for crude oils does not need to be super high, like in the cases of chemical, biological, or binding events detection, it still needs improvement. This can be achieved by improving the sensitivity, by using more sensitive nanoparticles to refractive index, or by reducing the noise. We think that one of the noises or the variations sources in the spectra is due to the nonuniform distribution of the particles on the substrate when immobilized by drop-coating, which can result in slight variation in the resonance. There are new ways that result in a more uniform distribution that can be used to improve the repeatability of the data. Also, the noise can be reduced by using higher resolution spectrometer.
- By using other nanoparticles with longer LSPR wavelengths and using longer excitation laser, it is possible to produce better SERS spectra that is more fluorescence-free and as a result, extra Raman bands could be seen.
- Integration with a microfluidic ship will make this approach more practical and appealing for inline real-time measurement.

For Terahertz spectroscopy

- The use of THz can be extended to measure the asphaltene yield curve and the asphaltene precipitation onset point

Bibliography

1. Speight, J. G. *The Chemistry and Technology of Petroleum,* 4th ed.; CRC Press (Taylor and Francis Group): Boca Raton, FL, 2007.

2. Nduagu, E.I. and Gates, I.D., 2015. Unconventional heavy oil growth and global greenhouse gas emissions. *Environmental science & technology*, *49*(14), pp.8824-8832.

3. Riazi, M.R. and Roomi, Y.A., 2001. Use of the refractive index in the estimation of thermophysical properties of hydrocarbons and petroleum mixtures. *Industrial & engineering chemistry research*, *40*(8), pp.1975-1984.

4. Yarranton, H.W., Okafor, J.C., Ortiz, D.P. and Van Den Berg, F.G.A., 2015. Density and refractive index of petroleum, cuts, and mixtures. *Energy & Fuels*, *29*(9), pp.5723-5736.

5. Taylor, S.D., Czarnecki, J. and Masliyah, J., 2001. Refractive index measurements of diluted bitumen solutions. *Fuel*, *80*(14), pp.2013-2018.

6. Chen, H., Kou, X., Yang, Z., Ni, W. and Wang, J., 2008. Shape-and size-dependent refractive index sensitivity of gold nanoparticles. *Langmuir*, *24*(10), pp.5233-5237.

7. Chen, H., Shao, L., Woo, K.C., Ming, T., Lin, H.Q. and Wang, J., 2009. Shape-dependent refractive index sensitivities of gold nanocrystals with the same plasmon resonance wavelength. *The Journal of Physical Chemistry C*, *113*(41), pp.17691-17697.

8. Chen, H., Shao, L., Li, Q. and Wang, J., 2013. Gold nanorods and their plasmonic properties. *Chemical Society Reviews*, *42*(7), pp.2679-2724.

9. Kharrat, A.M., Indo, K. and Mostowfi, F., 2013. Asphaltene content measurement using an optical spectroscopy technique. *Energy & Fuels*, *27*(5), pp.2452-2457.
10. ASTM D 3279, Standard Test Method for n-Heptane Insolubles; American Society for Testing and Materials (ASTM): West Conshohocken, PA, 2007.

11. ASTM D 6560, *Standard Test Method for Determination of Asphaltenes (Heptane Insolubles) in Crude Petroleum and Petroleum Products*; ASTM International: West Conshohocken, PA, 2000.

12. Wang, J.; Buckley, J. *Standard Procedure for Separating Asphaltenes from Crude Oils*. Petroleum Recovery Research Center, 2002.

13. Jansen, C., Wietzke, S., Peters, O., Scheller, M., Vieweg, N., Salhi, M., Krumbholz, N., Jördens, C., Hochrein, T. and Koch, M., 2010. Terahertz imaging: applications and perspectives. *Applied optics*, *49*(19), pp.E48-E57.

14. Shen, Y.C., Lo, A.T., Taday, P.F., Cole, B.E., Tribe, W.R. and Kemp, M.C., 2005. Detection and identification of explosives using terahertz pulsed spectroscopic imaging. *Applied Physics Letters*, *86*(24), p.241116.

15. Yu, C., Fan, S., Sun, Y. and Pickwell-MacPherson, E., 2012. The potential of terahertz imaging for cancer diagnosis: A review of investigations to date. *Quantitative imaging in medicine and surgery*, *2*(1), p.33.

16. Zhang, Y., Qiao, S., Liang, S., Wu, Z., Yang, Z., Feng, Z., Sun, H., Zhou, Y., Sun, L., Chen, Z. and Zou, X., 2015. Gbps terahertz external modulator based on a composite metamaterial with a double-channel heterostructure. *Nano letters*, *15*(5), pp.3501-3506.

17. Baxter, J.B. and Guglietta, G.W., 2011. Terahertz spectroscopy. *Analytical chemistry*, *83*(12), pp.4342-4368.

18. Plusquellic, D.F., Siegrist, K., Heilweil, E.J. and Esenturk, O., 2007. Applications of terahertz spectroscopy in biosystems. *ChemPhysChem*, *8*(17), pp.2412-2431.

19. Jepsen, P.U., Cooke, D.G. and Koch, M., 2011. Terahertz spectroscopy and imaging–Modern techniques and applications. *Laser & Photonics Reviews*, *5*(1), pp.124-166.

20. BP. *BP Statistical Review of World Energy 2016*; BP: London, U.K., 2016.

21. BP. *BP Energy outlook 2017 edition*; BP: London, U.K., 2017.

22. Ryder, A.G., 2005. Analysis of crude petroleum oils using fluorescence spectroscopy. In *Reviews in Fluorescence 2005* (pp. 169-198). Springer US.

23. Aske, N., Kallevik, H. and Sjöblom, J., 2001. Determination of saturate, aromatic, resin, and asphaltenic (SARA) components in crude oils by means of infrared and near-infrared spectroscopy. *Energy & Fuels*, *15*(5), pp.1304-1312.

24. Orrego-Ruiz, J.A., Guzmán, A., Molina, D. and Mejía-Ospino, E., 2011. Mid-infrared Attenuated Total Reflectance (MIR-ATR) predictive models for asphaltene contents in vacuum residua: asphaltene structure–functionality correlations based on Partial Least-Squares Regression (PLS-R). *Energy & Fuels*, *25*(8), pp.3678-3686.

25. Pasquini, C. and Bueno, A.F., 2007. Characterization of petroleum using near-infrared spectroscopy: Quantitative modeling for the true boiling point curve and specific gravity. *Fuel*, *86*(12), pp.1927-1934.

26. Kiefer, J., 2015. Recent advances in the characterization of gaseous and liquid fuels by vibrational spectroscopy. *Energies*, *8*(4), pp.3165-3197.

27. Chung, H. and Ku, M.S., 2000. Comparison of near-infrared, infrared, and Raman spectroscopy for the analysis of heavy petroleum products. *Applied spectroscopy*, *54*(2), pp.239-245.

28. Wilkinson, T.G., Clarkson, J., White, P.C., Meakin, N. and McDonald, K., 2013, May. Development of surface enhanced Raman scattering (SERS) spectroscopy monitoring of fuel markers to prevent fraud. In *Proc. of SPIE Vol* (Vol. 8710, pp. 87100G-1).

29. Andrews, A.B., Wang, D., Marzec, K.M., Mullins, O.C. and Crozier, K.B., 2015. Surface enhanced Raman spectroscopy of polycyclic aromatic hydrocarbons and molecular asphaltenes. *Chemical Physics Letters*, *620*, pp.139-143.

30. Zhan, H., Wu, S., Bao, R., Ge, L. and Zhao, K., 2015. Qualitative identification of crude oils from different oil fields using terahertz time-domain spectroscopy. *Fuel*, *143*, pp.189-193.

31. Jiang, C., Zhao, K., Zhao, L.J., Jin, W.J., Yang, Y.P. and Chen, S.H., 2014. Probing disaggregation of crude oil in a magnetic field with terahertz time-domain spectroscopy. *Energy & Fuels*, *28*(1), pp.483-487.

32. Jiang, C., Zhao, K., Fu, C. and Xiao, L., 2017. Characterization of Morphology and Structure of Wax Crystals in Waxy Crude Oils by Terahertz Time-Domain Spectroscopy. *Energy & Fuels*, *31*(2), pp.1416-1421.

33. Jin, W.J., Zhao, K., Yang, C., Xu, C.H., Ni, H. and Chen, S.H., 2013. Experimental measurements of water content in crude oil emulsions by terahertz time-domain spectroscopy. *Applied Geophysics*, *10*(4), p.506.

34. Song, Y., Zhan, H.L., Zhao, K., Miao, X.Y., Lu, Z.Q., Bao, R.M., Zhu, J. and Xiao, L.Z., 2016. Simultaneous characterization of water content and distribution in high-water-cut crude oil. *Energy & Fuels*, *30*(5), pp.3929-3933.

35. Al-Douseri, F.M., Chen, Y. and Zhang, X.C., 2006. THz wave sensing for petroleum industrial applications. *International journal of infrared and millimeter waves*, *27*(4), pp.481-503.

36. Tian, L., Zhou, Q., Jin, B., Zhao, K., Zhao, S., Shi, Y. and Zhang, C., 2009. Optical property and spectroscopy studies on the selected lubricating oil in the terahertz range. *Science in China Series G: Physics Mechanics and Astronomy*, *52*(12), pp.1938-1943.

37. Ikeda, T., Matsushita, A., Tatsuno, M., Minami, Y., Yamaguchi, M., Yamamoto, K., Tani, M. and Hangyo, M., 2005. Investigation of inflammable liquids by terahertz spectroscopy. *Applied Physics Letters*, *87*(3), p.034105.

38. Zhan, H., Zhao, K., Zhao, H., Li, Q., Zhu, S. and Xiao, L., 2016. The spectral analysis of fuel oils using terahertz radiation and chemometric methods. *Journal of Physics D: Applied Physics*, *49*(39), p.395101.

39. Ge, L.N., Zhan, H.L., Leng, W.X., Zhao, K. and Xiao, L.Z., 2015. Optical characterization of the principal hydrocarbon components in natural gas using terahertz spectroscopy. *Energy & Fuels*, *29*(3), pp.1622-1627.

40. Zhan, H., Zhao, K. and Xiao, L., 2015. Spectral characterization of the key parameters and elements in coal using terahertz spectroscopy. *Energy*, *93*, pp.1140-1145.

41. Giles, H. N.; Mills, C. O. Crude Oils: Their Sampling, Analysis, and Evaluation; ASTM International: West Conshohocken, PA, 2010.

42. Buckley, J.S., 1999. Predicting the onset of asphaltene precipitation from refractive index measurements. *Energy & Fuels*, *13*(2), pp.328-332.

43. Sieben, V.J., Molla, S., Mostowfi, F., Floquet, C.F., Speck, A. and Chau, K., 2017. Measuring Asphaltene Deposition Onset from Crude Oils Using Surface Plasmon Resonance. *Energy & Fuels*, *31*(6), pp.5891-5901.

44. Mullins, O.C., Pomerantz, A.E., Zuo, J.Y. and Dong, C., 2014. Downhole fluid analysis and asphaltene science for petroleum reservoir evaluation. *Annual review of chemical and biomolecular engineering*, *5*, pp.325-345.

45. Buckley, J.S. and Wang, J., 2002. Crude oil and asphaltene characterization for prediction of wetting alteration. *Journal of Petroleum Science and Engineering*, *33*(1), pp.195-202.

46. Castillo, J., Gutierrez, H., Ranaudo, M. and Villarroel, O., 2010. Measurement of the refractive index of crude oil and asphaltene solutions: onset flocculation determination. *Energy Fuels*, *24*(1), pp.492-495.

47. Zamora, V., Zhang, Z. and Meldrum, A., 2015. Refractometric sensing of heavy oils in fluorescent core microcapillaries. *Oil & Gas Science and Technology–Revue d'IFP Energies nouvelles*, *70*(3), pp.487-495.

48. Ooms, M.D., Fadaei, H. and Sinton, D., 2015. Surface plasmon resonance for crude oil characterization. *Energy & Fuels*, *29*(5), pp.3019-3023.

49. Melendez, L.V., Lache, A., Orrego-Ruiz, J.A., Pachon, Z. and Mejía-Ospino, E., 2012. Prediction of the SARA analysis of Colombian crude oils using ATR–FTIR spectroscopy and chemometric methods. *Journal of Petroleum Science and Engineering*, *90*, pp.56-60.

50. Hoepfner, M.P., Limsakoune, V., Chuenmeechao, V., Maqbool, T. and Fogler, H.S., 2013. A fundamental study of asphaltene deposition. *Energy & Fuels*, *27*(2), pp.725-735.

51. Adams, J.J., 2014. Asphaltene adsorption, a literature review. *Energy & Fuels*, *28*(5), pp.2831-2856.

52. Mullins, O.C., Sheu, E.Y., Hammami, A. and Marshall, A.G., 2007. *Asphaltenes, heavy oils, and petroleomics*. Springer Science & Business Media.

53. Mullins, O.C., Sabbah, H., Eyssautier, J., Pomerantz, A.E., Barré, L., Andrews, A.B., Ruiz-Morales, Y., Mostowfi, F., McFarlane, R., Goual, L. and Lepkowicz, R., 2012. Advances in asphaltene science and the Yen–Mullins model. *Energy & Fuels*, *26*(7), pp.3986-4003.

54. Ghosh, A.K., Chaudhuri, P., Kumar, B. and Panja, S.S., 2016. Review on aggregation of asphaltene vis-a-vis spectroscopic studies. *Fuel*, *185*, pp.541-554.

55. Andersen, S.I., del Rio, J.M., Khvostitchenko, D., Shakir, S. and Lira-Galeana, C., 2001. Interaction and solubilization of water by petroleum asphaltenes in organic solution. *Langmuir*, *17*(2), pp.307-313.

56. Khvostichenko, D.S. and Andersen, S.I., 2008. Interactions between asphaltenes and water in solutions in toluene. *Energy & Fuels*, *22*(5), pp.3096-3103.

57. Murgich, J., Merino-Garcia, D., Andersen, S.I., Manuel del Río, J. and Galeana, C.L., 2002. Molecular mechanics and microcalorimetric investigations of the effects of molecular water on the aggregation of asphaltenes in solutions. *Langmuir*, *18*(23), pp.9080-9086.

58. Gonzalez, V. and Taylor, S.E., 2016. Asphaltene adsorption on quartz sand in the presence of pre-adsorbed water. *Journal of colloid and interface science*, *480*, pp.137-145.

59. Riveros, L., Jaimes, B., Ranaudo, M.A., Castillo, J. and Chirinos, J., 2006. Determination of asphaltene and resin content in Venezuelan crude oils by using fluorescence spectroscopy and partial least squares regression. *Energy & fuels*, *20*(1), pp.227-230.

60. Sieben, V.J., Tharanivasan, A.K., Ratulowski, J. and Mostowfi, F., 2015. Asphaltenes yield curve measurements on a microfluidic platform. *Lab on a Chip*, *15*(20), pp.4062-4074.

61. Dreaden, E.C., Alkilany, A.M., Huang, X., Murphy, C.J. and El-Sayed, M.A., 2012. The golden age: gold nanoparticles for biomedicine. *Chemical Society Reviews*, *41*(7), pp.2740-2779.

62. Zhang, Q., Large, N. and Wang, H., 2014. Gold nanoparticles with tipped surface structures as substrates for single-particle surface-enhanced Raman spectroscopy: concave nanocubes, nanotrisoctahedra, and nanostars. *ACS applied materials & interfaces*, *6*(19), pp.17255-17267.

63. Atwater, H.A. and Polman, A., 2010. Plasmonics for improved photovoltaic devices. *Nature materials*, *9*(3), pp.205-213.

64. Wu, K.J., Chu, K.C., Chao, C.Y., Chen, Y.F., Lai, C.W., Kang, C.C., Chen, C.Y. and Chou, P.T., 2007. CdS nanorods imbedded in liquid crystal cells for smart optoelectronic devices. *Nano Letters*, *7*(7), pp.1908-1913.

65. Willets, K.A. and Van Duyne, R.P., 2007. Localized surface plasmon resonance spectroscopy and sensing. *Annu. Rev. Phys. Chem.*, *58*, pp.267-297.

66. Martinsson, E., Shahjamali, M.M., Large, N., Zaraee, N., Zhou, Y., Schatz, G.C., Mirkin, C.A. and Aili, D., 2016. Influence of surfactant bilayers on the refractive index sensitivity and catalytic properties of anisotropic gold nanoparticles. *small*, *12*(3), pp.330-342.

67. Maier, S.A., 2007. *Plasmonics: fundamentals and applications*. Springer Science & Business Media.

68. Sepúlveda, B., Angelomé, P.C., Lechuga, L.M. and Liz-Marzán, L.M., 2009. LSPR-based nanobiosensors. *Nano Today*, *4*(3), pp.244-251.

69. Ferraro, J.R., Nakamoto, K. and Brown, C.W., Introductory raman spectroscopy. 2003.

70. Abalde-Cela, S., Carregal-Romero, S., Coelho, J.P. and Guerrero-Martínez, A., 2016. Recent progress on colloidal metal nanoparticles as signal enhancers in nanosensing. *Advances in colloid and interface science*, *233*, pp.255-270.

71. Hao, E. and Schatz, G.C., 2004. Electromagnetic fields around silver nanoparticles and dimers. *The Journal of chemical physics*, *120*(1), pp.357-366.

72. Kneipp, K., Kneipp, H., Itzkan, I., Dasari, R.R. and Feld, M.S., 1999. Ultrasensitive chemical analysis by Raman spectroscopy. *Chemical reviews*, *99*(10), pp.2957-2976.

73. Wei, H., Abtahi, S.M.H. and Vikesland, P.J., 2015. Plasmonic colorimetric and SERS sensors for environmental analysis. *Environmental Science: Nano*, *2*(2), pp.120-135.

74. Mayes, J.R. and Nunnally, W.C., 1999, June. Analytical modelling of a linear GaAs photoconductive switch for short pulse excitation. In *Pulsed Power Conference, 1999. Digest of Technical Papers. 12th IEEE International* (Vol. 2, pp. 1207-1210). IEEE.

75. Tani, M., Matsuura, S., Sakai, K. and Nakashima, S.I., 1997. Emission characteristics of photoconductive antennas based on low-temperature-grown GaAs and semi-insulating GaAs. *Applied optics*, *36*(30), pp.7853-7859.

76. Jepsen, P.U., Jacobsen, R.H. and Keiding, S.R., 1996. Generation and detection of terahertz pulses from biased semiconductor antennas. *JOSA B*, *13*(11), pp.2424-2436.

77. Nguyen, T.K., Ho, T.A., Han, H. and Park, I., 2012. Numerical study of self-complementary antenna characteristics on substrate lenses at terahertz frequency. *Journal of Infrared, Millimeter, and Terahertz Waves*, *33*(11), pp.1123-1137.

78. Nahata, A., Weling, A.S. and Heinz, T.F., 1996. A wideband coherent terahertz spectroscopy system using optical rectification and electro-optic sampling. *Applied physics letters*, *69*(16), pp.2321-2323.

79. Gu, P., Chang, F., Tani, M., Sakai, K. and Pan, C.L., 1999. Generation of coherent cw-terahertz radiation using a tunable dual-wavelength external cavity laser diode. *Japanese journal of applied physics*, *38*(11A), p.L1246.

80. Zhang, J., Zhang, L. and Xu, W., 2012. Surface plasmon polaritons: physics and applications. *Journal of Physics D: Applied Physics*, *45*(11), p.113001.

81. Berry, C.W., Wang, N., Hashemi, M.R., Unlu, M. and Jarrahi, M., 2013. Significant performance enhancement in photoconductive terahertz optoelectronics by incorporating plasmonic contact electrodes. *Nature communications*, *4*, p.ncomms2638.

82. Jooshesh, A., Bahrami-Yekta, V., Zhang, J., Tiedje, T., Darcie, T.E. and Gordon, R., 2015. Plasmon-enhanced below bandgap photoconductive terahertz generation and detection. *Nano letters*, *15*(12), pp.8306-8310.

83. Fesharaki, F., Jooshesh, A., Bahrami-Yekta, V., Mahtab, M., Tiedje, T., Darcie, T.E. and Gordon, R., 2017. Plasmonic Anti-reflection Coating for Photoconductive Terahertz Generation. *ACS Photonics*.

84. Hajisalem, G., Min, Q., Gelfand, R. and Gordon, R., 2014. Effect of surface roughness on self-assembled monolayer plasmonic ruler in nonlocal regime. *Optics express*, *22*(8), pp.9604-9610.

85. Shao, L., Ruan, Q., Jiang, R. and Wang, J., 2014. Macroscale Colloidal Noble Metal Nanocrystal Arrays and Their Refractive Index-Based Sensing Characteristics. *Small*, *10*(4), pp.802-811.

86. Cunningham, P.D., Valdes, N.N., Vallejo, F.A., Hayden, L.M., Polishak, B., Zhou, X.H., Luo, J., Jen, A.K.Y., Williams, J.C. and Twieg, R.J., 2011. Broadband terahertz characterization of the refractive index and absorption of some important polymeric and organic electro-optic materials. *Journal of Applied Physics*, *109*(4), pp.043505-043505.

87. Brioude, A., Jiang, X.C. and Pileni, M.P., 2005. Optical properties of gold nanorods: DDA simulations supported by experiments. *The Journal of Physical Chemistry B*, *109*(27), pp.13138-13142.

88. Chen, C.D., Cheng, S.F., Chau, L.K. and Wang, C.C., 2007. Sensing capability of the localized surface plasmon resonance of gold nanorods. *Biosensors and Bioelectronics*, *22*(6), pp.926-932.

89. Homola, J., 2008. Surface plasmon resonance sensors for detection of chemical and biological species. *Chemical reviews*, *108*(2), pp.462-493.

90. Uy, D. and O'Neill, A.E., 2005. Principal component analysis of Raman spectra from phosphorus-poisoned automotive exhaust-gas catalysts. *Journal of Raman Spectroscopy*, *36*(10), pp.988-995.

91. Goual, L. and Firoozabadi, A., 2002. Measuring asphaltenes and resins, and dipole moment in petroleum fluids. *AIChE Journal*, *48*(11), pp.2646-2663.

92. Zhang, J. and Grischkowsky, D., 2004. Terahertz time-domain spectroscopy study of silica aerogels and adsorbed molecular vapors. *The Journal of Physical Chemistry B*, *108*(48), pp.18590-18600.

93. Tao, R. and Xu, X., 2006. Reducing the viscosity of crude oil by pulsed electric or magnetic field. *Energy & fuels*, *20*(5), pp.2046-2051.

94. Kar, T. and Hascakir, B., 2015. The role of resins, asphaltenes, and water in water–oil emulsion breaking with microwave heating. *Energy & Fuels*, *29*(6), pp.3684-3690.

Appendix A

```
%MATLAB code to calculate the refractive index and absorption of oil,

maltene and asphaltene:

c=299792458;
%.......  loading the data

load reference.csv;       x = reference(:,1);    r = reference(:,2);
load maltene.csv;         m = maltene(:,2);
load oil.csv;             o = oil(:,2);

%.......  Calculate FFt spectrum


Factor = 1;
period=199.980000E-12;                          % scanning time
L=length(x);
T=period/(L-1);
Fs=1/T;                                         % sampling frequency
nfft = L*Factor;                                % FFT factor
Halfnfft = ceil(nfft/2);
f=linspace(0,Fs*Halfnfft/nfft,Halfnfft)/1E12; % Frequecy vector in(THz)


rFFT = fft(r,nfft);      RFFT= rFFT(1:Halfnfft);
oFFT = fft(o,nfft);      OFFT= oFFT(1:Halfnfft);
mFFT = fft(m,nfft);      MFFT= mFFT(1:Halfnfft);

R = abs(RFFT);       R_phase=unwrap(angle(RFFT));
O = abs(OFFT);       O_phase=unwrap(angle(OFFT));
M = abs(MFFT);       M_phase=unwrap(angle(MFFT));

%.......  Refractive index calculation

A= %;                                % Inter the asphaltene % in the oil
V= A*1.2;                                          % asphaltene volume

n_oil =1+(R_phase-O_phase)./f*c/(2*pi*d); % oil refractive index
n_mal =1+(R_phase-M_phase)./f*c/(2*pi*d); % maltene refractive index
n_asp=(n_oil-(n_mal*(1-V)))/V;            % asphaltene refractive index


%.......  Absorption calculation

a_oil=-2*log( (O./R) *((1+n_oil)^2 )./(4*n_oil) );  %oil absorption
a_mal=-2*log( (M./R).*((1+n_mal)^2 )./(4*n_mal) );  %maltene absorption
a_asp= a_oil-a_mal;                                 %asphaltene absorption
```